An *In Vivo* Analysis of the Functional Motifs of DEAD-box RNA Helicase Me31B in *Drosophila* Fertility and Germline Development

Evan Kara[1], Aidan McCambridge[1], Megan Proffer[1], Carol Dilts[1], Brooke Pumnea[1], John Eshak[1], Korey A. Smith[1], Isaac Fielder[1], Dominique A. Doyle[2], Bianca M. Ortega[2], Yousif Mukatash[1], Noor Malik[1], Ammaar R. Mohammed[1], Deep Govani[1], Matthew G. Niepielko[2,3], and Ming Gao[1,*]

1. Biology Department, Indiana University Northwest, Gary, IN, USA
2. School of Integrative Science and Technology, Kean University, Union, NJ, USA
3. Department of Biological Sciences, Kean University, Union, NJ, USA

***Correspondence**

M. Gao, Biology Department, Marram Hall 310, 3400 Broadway, Gary, IN 46408, USA

Fax: +1 219 980 7125

Tel: +1 219 980 6722

Email: minggao@iun.edu

Abstract

In the *Drosophila* germline, Me31B is a putative ATP-dependent, RNA helicase that plays an important role in post-transcriptional RNA regulation to ensure mRNA's correct

spatial and temporal expression, a process crucial for proper germline development and fertility. However, Me31B's *in vivo* working mechanism remains unclear. In this study, we aim to analyze the functions of Me31B's key domains/motifs to understand how these domains/motifs operate to fulfill the protein's overall activities. We generated mutant *Drosophila* strains for six important motifs including three ATPase/helicase motifs (DEAD-box, DVLARAK, and HRIGR), the N-terminal domain (N-ter), the C-terminal domain (C-ter), and a protein-binding motif (FDF motif-binding motif). In characterizing these mutants, we observed that the three ATPase/helicase motif mutations cause dominant female sterility, which is associated with developmental defects in oogenesis and embryogenesis. Follow-up examinations of the DVLARAK motif mutant revealed abnormalities in germline mRNA localization and transcript level. The Me31B N-ter domain (deletion of C-ter), C-ter domain (deletion of N-ter), and mutation of the FDF motif-binding motif led to a decrease in female fertility and abnormal subcellular Me31B localizations within the egg chambers. Moreover, deletion of Me31B's N-ter or C-ter motif decreases Me31B protein levels in the ovaries. This study indicates that these six motifs of Me31B play distinct roles in contributing to Me31B's whole-protein functions such as ATPase, RNA helicase, protein stability, protein localization, and partner protein binding, crucial for germline development and fertility. Considering the Me31B protein family's conserved presence in both *Drosophila* germline and soma and in other eukaryotes such as yeast, worms, mice, and humans, the results from this study could expand our understanding of Me31B family helicases' general working mechanisms in different cell types and species.

Introduction

Drosophila Me31B is an evolutionarily conserved, ATP-dependent, DEAD-box RNA helicase that is important for *Drosophila* germline development and fertility [1-5], with homologs like CGH-1 (worms) [6, 7], DjCBC-1 (planarians) [8, 9], Xp54 (frogs) [10, 11], p54 (mice) [12, 13], and DDX6/Rck (humans) [14-18] playing similar roles in diverse animal species. In these animals, the main role of Me31B family helicases lies in their post-transcriptional RNA regulation including RNA storage, transportation, translational regulation, stabilization, and decay, which ensure the expression of the messages at the correct time and location, and leads to proper germline functionality and development [14, 19-23].

Drosophila Me31B has been employed as a valuable model to study the helicases in the family. Me31B's necessity in the *Drosophila* germline has been underscored by *me31B's* loss-of-function mutation or strong knockdown (KD) causing severe egg chamber development defects or early oogenesis arrest, respectively [1, 24]. In normal egg chambers, Me31B proteins are expressed and aggregated into ribonucleoprotein (RNP) complexes, granular assemblies of proteins and RNAs. In these granules, Me31B interacts with other partner proteins such as Tral (a translational repressor protein that usually complexes with Me31B in various types of RNP granules) to render post-transcriptional controls on the contained RNAs, a process necessary for proper germline development [3, 25-29]. So far, our understanding of Me31B function mostly came from using *Drosophila* strains with complete *me31B* loss-of-function alleles, strains with a significant decrease of Me31B protein level, or biochemical analysis of the protein *in vitro*. Therefore, the protein's molecular-level working mechanism *in vivo* has

67 remained unclear. In this study, we aim to analyze the *in vivo* functions of important
68 domains/motifs of Me31B and then understand how they fit together to contribute to
69 Me31B's whole-protein activities.

70 This study focuses on six Me31B domain/motifs (domains and motifs will be called
71 motifs from here for simplicity): DEAD-box motif (AA 207–210), DVLARAK motif (AA
72 97–103), HRIGR motif (AA 381–385), N-ter motif (AA 1–267), C-ter motif (AA 268–459),
73 and FDF motif-binding motif (AA 285–289). Previous research suggests that the first
74 three motifs (DEAD-box, DVLARAK, and HRIGR) are crucial for the ATPase/helicase
75 activities of Me31B [30-32]; the two large N-ter and C-ter motifs each contain a RecA-
76 like domain and participate in a broad spectrum of activities including ATPase/helicase,
77 protein binding, and assembly into RNP granules [19, 30, 33]; and the FDF motif-
78 binding motif enables Me31B to physically bind to the FDF motifs on translational
79 repressor partners such as Tral or EDC3 [33-36]. To study these motifs' *in vivo*
80 functions, we used the CRISPR gene-editing technique to create *Drosophila* strains
81 carrying point mutations that disrupt the motifs' functions or deletion mutations in the
82 *me31B* genes (Figure 1). Phenotype characterization of the mutants' germline revealed
83 that the six motifs are important for *Drosophila* fertility and germline development while
84 playing different molecular-level roles in localizing germline RNA, maintaining germline
85 RNA level, and stabilizing and localizing Me31B proteins.
86

87 Results and Discussions

88 **Me31B ATPase/helicase motif mutations lead to dominant female sterility.**

89 Although structural and functional studies on Me31B and its homologs identified several

90 ATPase/helicase motifs in Me31B and suggested these motifs' potential functions in
91 ATP hydrolysis, RNA binding, and RNA translational regulation [11, 19, 30, 32, 34, 37,
92 38], the *in vivo* functions of the motifs have not been investigated. To study this, we
93 introduced single or multiple point mutations to three conserved ATPase/helicase motifs
94 individually: E208A for DEAD box motif (D**E**AD→D**A**AD), R101A and K103A for
95 DVLARAK motif (DVLA**R**A**K**→DVLA**A**A**A**), and R385Q for HRIGR motif
96 (HRIG**R**→HRIG**Q**). The resulting *me31B* alleles are *me31B*^{E208A}, *me31B*^{DVLAAAA}, and
97 *me31B*^{R385Q}, respectively (illustrated in Figure 1). The introduced mutations were
98 reported to disrupt the motifs' normal functions in Me31B homologs or structurally
99 similar proteins [30-32, 38-41]. When maintaining the three mutant strains, we
100 immediately noticed that all three alleles dominantly cause female sterility. Specifically,
101 *me31B*^{E208A}/+, *me31B*^{DVLAAAA}/+, and *me31B*^{R385Q}/+ heterozygous female flies do not
102 produce any viable progeny in the presence of males from the wildtype *w*^{1118} strain. In
103 contrast, *me31B*^{E208A}/+, *me31B*^{DVLAAAA}/+, and *me31B*^{R385Q}/+ heterozygous male flies
104 were able to fertilize *w*^{1118} females and produce viable progenies bearing the mutant
105 *me31B* alleles, suggesting that the three *me31B* alleles cause sterility in females only.

106 To find out what caused the sterility, we first checked *me31B*^{E208A}/+, *me31B*^{DVLAAAA}/+,
107 and *me31B*^{R385Q}/+ strains for their embryo laying, development, and morphology.
108 Although embryo laying was observed from all three strains, none (0%) of their embryos
109 (n = 541 for *me31B*^{E208A}/+, n = 100 for *me31B*^{DVLAAAA}/+, and n = 17 for *me31B*^{R385Q}/+)
110 were able to develop to larva or later stages on grape agar plates (see Materials and
111 Methods for the hatchability assay conditions). A closer examination of the un-hatched
112 embryos from the three mutants showed that 78% of the embryos from *me31B*^{E208A}/+,

113 33% of the embryos from *me31B*^{DVLAAAA}/+, and 100% of the embryos from
114 *me31B*^{R385Q}/+ had one or more types of patterning defects like fused, very short, or no
115 dorsal appendages (Figure 2A), consistent with the strains being sterile. Among the
116 three strains, *me31B*^{R385Q}/+ showed the most severe phenotype: they laid few embryos,
117 and all the embryos laid had severe egg-shell shape defects along with the complete
118 absence of dorsal appendages (Figure 2A).

119 The embryonic defects in the three mutants indicate that their oogenesis did not
120 proceed normally, so we examined their ovaries. In *me31B*^{E208A} and *me31B*^{DVLAAAA}
121 mutant ovaries, we observed defects in nurse cell dumping, a process in which the
122 nurse cells completely expel all their cytoplasm into late-stage eggs (reviewed in [42]).
123 In the *me31B*^{E208A} mutant, 52% of the stage-14 eggs (n = 13) were still connected with
124 egg chamber tissues that contain nurse cell materials (Figure 2B), indicating incomplete
125 nurse cell dumping. This “dumpless” phenotype is more prominent in *me31B*^{DVLAAAA}
126 mutant: approximately 78% of *me31B*^{DVLAAAA} stage-14 egg chambers (n = 32) did not
127 complete dumping, and the “un-dumped” egg chamber regions were larger than that in
128 the *me31B*^{E208A} mutant (Figure 2C). Consistent with this egg development defect, the
129 *me31B*^{DVLAAAA} mutant showed reduced egg laying compared to the wildtype control
130 (Supplementary Figure 1). These phenotypes mimic previously reported dumpless
131 phenotypes in the *dcp-1* (encoding a caspase involved in apoptosis) mutant egg
132 chambers, leading to decreased egg laying and early embryo development arrest [43].
133 The *dcp-1* mutation-induced dumpless phenotypes and sterility were associated with
134 abnormal nucleus envelope breakdown and cytoskeleton organization during nurse cell
135 apoptosis and dumping [43]. Whether the same mechanism is involved in the

136 *me31B*^{E208A} and *me31B*^{DVLAAAA} mutations remains to be analyzed. The most severe
137 oogenesis defects were observed in the *me31B*^{R385Q} mutant. We observed frequent egg
138 chamber degenerations at early-to-mid stages (Figure 2D), consistent with this mutant's
139 few egg lay and sterility.

140 The sterility and defects in oogenesis and embryogenesis in all three mutants suggest
141 that each ATPase/helicase motif is needed for *Drosophila* germline growth, and their
142 cooperative actions are likely needed to output the correct ATPase/helicase function. An
143 explanation for these mutations being dominant could be that the mutations introduced
144 detrimental functions that lead to the mutant Me31B protein being "toxic" to germline
145 cells. This explanation is supported by previous research on similar mutations in other
146 RNA helicases. For example, in eIF4A, another DEAD-box RNA helicase essential for
147 germline mRNA translational control [44, 45], D**E**AD→D**Q**AD and HRIG**R**→HRIG**Q**
148 mutations cause the protein to become dominant negative in translation *in vitro* [46, 47].
149 As another example, in an assay of Xp54 (Me31B homolog in *Xenopus*)'s effect on
150 tethered RNAs, D**E**AD→D**Q**AD mutation, DILA**R**A**K** (homologous to DVLARAK in
151 Me31B)→DILA**A**A**A** mutation, and HRIG**R**→HRIG**Q** mutations changed the protein's
152 regulation on the RNA from translational repression to translational activation [30].
153 These reports made us postulate that the dominant sterility effects of *me31B*^{E208A},
154 *me31B*^{DVLAAAA}, and *me31B*^{R385Q} mutations may be caused by altered RNA translational
155 control activity of the mutated proteins.

156 It is integral to note that the HRIG**R**→HRIG**Q** mutation caused much more severe
157 germline phenotypes than the D**E**AD→D**A**AD or DVLA**R**A**K**→DVLA**A**A**A** mutations. We
158 suspect this may be either that 1) substituting an ATPase/helicase motif's key amino

159 acid (like arginine, R) to glutamine (Q) causes more detrimental effects than alanine (A),
160 or that 2) the HRIGR motif plays separate and more significant roles than the DEAD and
161 DVLARAK motifs. Previous research in other systems provided conceptual support for
162 both explanations. For the first argument, D**Q**AD mutation in the DEAD-box motif of
163 GLH-1 (a conserved germ granule RNA helicase in *C. elegans*) led to a more severe
164 fertility decrease and embryo arrest phenotypes than D**A**AD mutation [48, 49]. For the
165 second, D**E**AD→D**Q**AD mutation in the DEAD-box helicase eIF4A abolish the protein's
166 ATPase activity but retain a small amount of RNA-binding activity, while the
167 HRIG**R**→HRIG**Q** mutation abolishes RNA-binding ability but retains some ATPase
168 activity [46], suggests that the HRIGR motif may perform unique steps/roles in the
169 helicase's enzymatic actions.
170

171 **Me31B helicase activity functions in *nos* localization by modulating *osk* and *nos***
172 **transcript levels**

173 Considering Me31B's known role in post-transcriptional RNA regulation on important
174 germline mRNAs such as *nanos* (*nos*), we investigated whether the above
175 ATPase/helicase mutations affect *nos* localization to its germ plasm destination in late-
176 stage eggs (germ plasm is a special cytoplasm at the posterior pole of late-stage eggs
177 and early embryos; germ plasm contains mRNAs needed for processes including
178 embryo patterning and germ cell formation. For reviews, see [50-54]). Normal *nos*
179 localization occurs through the Oskar-dependent formation of homotypic clusters within
180 germ granules, aggregates that contain multiple copies of *nos* transcripts [55, 56]. We
181 tested this hypothesis with the *me31B*^{DVLAAAA}/+ strain and performed single-molecule

182 fluorescent *in situ* hybridization (smFISH) on stage 13 oocytes to identify both
183 unlocalized *nos* transcripts and *nos* clusters in the posterior germ plasm. Using
184 previously established imaging and image analysis techniques [55, 56] (See Material
185 and Methods), we quantified the number of *nos* transcripts that reside within homotypic
186 clusters in the *me31B*^{DVLAAAA} mutant and a control CRISPR strain (*me31B*^{WT}*-GFP*) with
187 wildtype *me31B* gene (Figure 3A). We found that the average number of *nos* transcripts
188 found in a homotypic cluster of the control was 6.42 ± 0.47 transcripts per cluster which
189 were not significantly different from the previously published average of 7.58 ± 0.42
190 transcript per *nos* cluster in the *yellow white* flies ($p = 0.12$) [56], suggesting that our
191 CRISPR genome modifications like adding the GFP tag do not affect *nos* localization.
192 However, in the *me31B*^{DVLAAAA} mutant, the average number of *nos* transcripts found in a
193 homotypic cluster is 2.33 ± 0.21, a significant reduction compared to the *me31B*^{WT}*-GFP*
194 control ($p < 0.0001$). Together, these data suggest that the Me31B helicase activity
195 influences *nos* localization to the posterior germ plasm.

196 We next explored the mechanisms by which Me31B influences *nos* localization.
197 Recently, it has been shown using computational modeling and experimental validation
198 that the localization of *nos* is influenced by 1) the number of *nos* transcripts that are
199 expressed, 2) the amount of Osk in the system, and 3) *nos*'s clustering factor, a
200 quantifiable effect that, in conjunction with *nos* transcript and Osk levels, regulates the
201 number of transcripts that can accumulate within a homotypic cluster [56, 57]. To
202 identify whether *me31B*^{DVLAAAA} affects one or more of these mechanisms, we first
203 conducted RT-PCR to measure the level of *nos* and *osk* RNAs in the system. We found
204 that *nos* transcript levels were reduced to 61% ± 7% of wild-type levels and *osk* levels

205 were reduced to 56% ± 4% when compared to wild-type (Figure 3C). To determine
206 whether these changes can account for the observed reduction of *nos* homotypic cluster
207 sizes in the *me31B*^{DVLAAAA} mutant, we used computational modeling to recapitulate *nos*
208 localization *in silico* by adjusting a previously published model's parameters [57] from
209 1.00 to 0.61 for *nos* transcript levels and from 1.00 to 0.56 for Osk levels (See Material
210 and methods). Modeled *nos* homotypic clusters contained an average of 2.86
211 transcripts per cluster, which was not significantly different from the average produced
212 by the *me31B*^{DVLAAAA} mutant ($p = 0.988$) (Figure 3B). Together, these data suggest that
213 the mechanism creating the *nos* localization defect in the *me31B*^{DVLAAAA} mutant is
214 caused by a combined effect generated by the reduction of *nos* and *osk* levels.

215 Me31B is a known component of an ATP-dependent assembly of a stable, repressed
216 ribonucleoprotein particle (RNP) containing *nos* [3, 22]. In the *me31B*^{DVLAAAA} mutant,
217 ATP-dependent helicase activity is presumably disrupted, causing a reduction of *nos*
218 transcripts (Figure 3C). Combining our new data with previous findings that Me31B
219 functions in post-transcriptional mRNA regulation like RNA stability control [1-3, 28, 36],
220 we suggest that Me31B functions in stabilizing unlocalized RNPs containing *nos* and
221 *osk*, allowing for stable mRNAs to reach and become incorporated into the germ plasm.
222 Furthermore, we suggest that disruption of the DVLARAK motif results in a
223 destabilization of mRNAs that have not localized to the germ plasm, and a subsequent
224 decrease in *nos* and *osk* that are available to form the germ plasm and ultimately
225 reducing the *nos* localization. Additional germ plasm mRNAs such as *cycB*, *pgc*, and *gcl*
226 also diffuse to the posterior RNPs containing a single transcript and form homotypic
227 clusters within germ granules [55]. Thus, future studies should explore whether

228 Me31B's helicase activity is specific to *nos* or has a more global role in stabilizing
229 unlocalized germ plasm mRNAs. We measured the transcript levels to determine
230 whether *nos* and *osk* transcript levels changed in the other two ATPase/helicase
231 mutants (*me31B*^{E208A}/+ and *me31B*^{R385Q}/+). To our surprise, in *me31B*^{E208A}/+ flies, *nos*
232 level remains comparable (104% ± 7%) to the *w*^{1118} control strain, while *osk* mRNA level
233 is significantly up-regulated (162% ± 12%) (Figure 3D). In *me31B*^{R385Q}/+ flies, *nos*
234 mRNA showed a significant decrease (44% ± 2%), while *osk* level showed a significant
235 increase (194% ± 12%) compared to the control (Figure 3E). Comparing the changes of
236 *nos* and *osk* between the three ATPase/helicase mutants (compare Figure 3C, D, and
237 E), we found that the three dominant-sterile mutations caused nonuniform effects on the
238 levels of *nos* and *osk*. This suggests that the three motifs play different roles in
239 maintaining germline mRNA levels or responsible for maintaining different RNAs. From
240 this, we further suggest that the change of *nos* and *osk* levels cannot be the only cause
241 for the sterility of the three mutants. Further studies are needed to reveal and contrast
242 how different ATPase/helicase motif mutations globally affect germline RNAs.
243

244 **Me31B N-ter motif, C-ter motif, and FDF motif-binding motif mutations decrease**
245 **female fertility**

246 We next analyzed the functions of the Me31B N-ter motif (AA 1–267), C-ter motif (AA
247 268–459), and FDF motif-binding motif (AA 285–289). The N-ter motif contains a RecA-
248 like domain and contributes to the protein's ATP binding, helicase activity, and P-body
249 assembly ability [19, 30]. The C-ter motif also contains a RecA-like domain and
250 contributes to the protein's ATP hydrolysis, helicase activity, RNA translational

251 repression, partner-protein binding, and P-body assembly ability [30, 33, 35, 58]. The
252 FDF motif-binding motif allows Me31B to physically interact with FDF motifs in other
253 proteins such as Tral and EDC3 [3, 4, 28, 33, 34, 36]. To study these motifs'
254 contributions to Me31B whole-protein activities, we generated *me31B*$^{N\text{-}ter}$, *me31B*$^{C\text{-}ter}$,
255 *me31B*^{FDF}, and *me31B*^{WT} alleles which contain the N-ter coding sequence, the C-ter
256 coding sequence, point mutations in the FDF motif-binding motif, and wildtype *me31B*
257 gene (as control), respectively (illustrated in Figure 1). We do note that our attempts to
258 generate the original N-ter (AA 1 - 267) and C-ter (AA 268 - 459) mutations were
259 hindered by technical difficulties, but we were able to generate N-ter (AA 1 - 276) and
260 C-ter (AA 277 - 459) mutations instead, so the latter constructs were used in this study.
261 We first screened the mutants homozygous for the three alleles (*me31B*$^{N\text{-}ter}$, *me31B*$^{C\text{-}ter}$,
262 and *me31B*^{FDF}) for their fertility by using a previously reported female fertility assay [59].
263 In this assay, the egg laying and progeny production (hatchability) were separately
264 analyzed to yield a more complete understanding of how fertility was affected in these
265 mutants. The assay showed that *me31B*$^{N\text{-}ter}$, *me31B*$^{C\text{-}ter}$, and *me31B*^{FDF} mutant females
266 showed a significant fertility decrease compared to the *me31B*^{WT} control (Figure 4A).
267 Specifically, in the egg laying part of the assay, a *me31B*^{WT} control female fly laid an
268 average of 117 eggs during the assay period, while a *me31B*$^{N\text{-}ter}$, *me31B*$^{C\text{-}ter}$, and
269 *me31B*^{FDF} fly laid an average of 68, 29, and 77 eggs, respectively, a significant
270 decrease of 42.9%, 75.2%, and 34.2%, respectively (Figure 4A). In the progeny
271 production part, a *me31B*^{WT} control female produced an average of 106 progeny flies. In
272 contrast, a *me31B*$^{N\text{-}ter}$, *me31B*$^{C\text{-}ter}$, and *me31B*^{FDF} fly produced 47, 0, and 75 progenies,
273 a significant decrease of 55.7 % and 100% and an insignificant decrease of 29.2%,

274 respectively (Figure 4B). The apparent absence of progeny from the *me31B*$^{C\text{-}ter}$ mutant
275 indicated that the *me31B*$^{C\text{-}ter}$ females were sterile. To validate this, we collected the
276 eggs (n = 97) from *me31B*$^{C\text{-}ter}$ females (accompanied by *w*^{1118} males) on grape-juice
277 agar plates and examined the eggs' development. We observed that none of the eggs
278 developed to larva or later stages and that all the eggs showed morphological defects
279 including fused dorsal appendages (n = 66, 68% of the eggs) or no dorsal appendages
280 (n = 31, 32% of the eggs) (Figure 4D), consistent with *me31B*$^{C\text{-}ter}$ females being sterile.

281 We calculated the egg hatchability rate of the three mutants by dividing the number of
282 viable progenies by the number of eggs laid. The hatchability rates of *me31B*$^{N\text{-}ter}$ and
283 *me31B*$^{C\text{-}ter}$ strains are 68.3% and 0%, respectively, a significant decrease compared to
284 the control's 90.8% hatchability rate (Figure 4C). For the *me31B*^{FDF} strain, the
285 hatchability (97.1%) is not significantly different from the control (Figure 4C).

286 We conclude that Me31B's N-ter or C-ter motifs (when expressed alone) and mutation
287 in the FDF motif-binding motif cause *Drosophila* female fertility to decrease. Particularly,
288 the *me31B*$^{N\text{-}ter}$ mutant and *me31B*$^{C\text{-}ter}$ mutant cause defects in both egg laying quantity
289 and egg hatchability. However, we cannot neglect that the sterility of the *me31B*$^{C\text{-}ter}$
290 mutant is a more substantial fertility defect than the *me31B*$^{N\text{-}ter}$ mutant, suggesting the
291 two domains' different importance in maintaining fertility. Considering that *me31B* is an
292 essential gene and its loss-of-function mutations are lethal [1], we were surprised to see
293 that either Me31B N-ter or C-ter motif (when expressed alone) is enough to support fly
294 viability, suggesting that either motif can provide certain essential, full-length-protein
295 functions that enable *Drosophila* growth. Comparatively, the *me31B*^{FDF} strain showed a
296 minor fertility decrease with no measurable defects in egg hatchability. This means that

297 the disruption of Me31B's FDF-motif binding function has a mildly negative effect on
298 fertility.
299

300 **Me31B N-ter motif and C-ter motif mutations decrease Me31B protein level.**
301 To follow up with the fertility defects in the *me31B*$^{N\text{-}ter}$, *me31B*$^{C\text{-}ter}$, and *me31B*^{FDF}
302 mutants, we hypothesize that these mutations may have changed Me31B protein
303 stability and reduced the amount of protein in the germline. To test this, we took
304 advantage of the GFP tags fused to the wildtype and mutant Me31B proteins and used
305 anti-GFP Western blots to quantify the proteins in the ovaries of the mutant strains. We
306 observed that the Me31B$^{N\text{-}ter}$ and Me31B$^{C\text{-}ter}$ protein levels are 40% and 11% of the
307 Me31B^{WT} control, respectively (Figure 5A and 5B). The Me31B^{FDF} protein level (114%)
308 is comparable to the Me31B^{WT} control. We conclude that the N-ter and C-ter motifs are
309 essential for maintaining the Me31B protein level and deleting either half of the protein
310 likely destabilized the protein. We also suggest that the Me31B$^{C\text{-}ter}$ protein (N-terminal
311 deletion) is even less stable than the Me31B$^{N\text{-}ter}$ protein (C-terminal deletion). Together
312 with the fertility experiments (Figure 4), we noticed that the mutant strains' fertility and
313 their mutant protein expression levels share a similar trend: *me31B*$^{C\text{-}ter}$ mutant showing
314 complete sterility and the least level of protein expression and *me31B*^{FDF} mutant
315 showing a mild fertility decrease and near wild type-level protein expression (compare
316 Figure 4 and Figure 5B). We speculate that, besides the protein functions that were
317 likely altered, the change of Me31B protein abundance could be a factor influencing the
318 fertility of the mutants.
319

320 **Me31B N-ter motif, C-ter motif, and FDF motif-binding motif mutations alter**
321 **Me31B subcellular localization**

322 Me31B is abundantly expressed in the cytoplasm of nurse cells and developing oocytes
323 in *Drosophila* ovaries. In these cells, Me31B complexes with partner protein Tral, and
324 aggregate together into RNP granules including perinuclear granules (nuage granules)
325 in nurse cells, P-body/sponge body granules in nurse cells and oocytes, and germ
326 plasm granules in oocytes [1, 24, 28]. To determine whether the *me31B*$^{N\text{-}ter}$, *me31B*$^{C\text{-}ter}$,
327 and *me31B*^{FDF} mutations affect Me31B subcellular localization, we used the GFP-tags
328 on the Me31B proteins to visualize them in the ovary cells and used anti-Tral
329 immunostaining to mark the RNP granules.

330 In the early-stage egg chambers (Figure 6A), wildtype Me31B^{WT}-GFP and Tral both
331 localize to the nuage granules and the P body/sponge body granules in the nurse cells
332 and developing oocytes (Figure 6A, first row). The two proteins showed extensive
333 overlap at these granules, suggesting likely colocalization. This localization pattern of
334 Me31B^{WT}-GFP and Tral is indistinguishable from the wildtype proteins in Oregon-R
335 strains or GFP-Trap strains carrying wildtype *me31B* genes [1, 24]. However, in
336 *me31B*$^{N\text{-}ter}$, *me31B*$^{C\text{-}ter}$, and *me31B*^{FDF} egg chambers, the three mutant Me31B-GFP
337 proteins were conspicuously more diffused in the nurse cells and oocytes, and they no
338 longer overlap with Tral, whose localization remains similar to that in the *me31B*^{WT}
339 control (Figure 6A, three bottom rows). This indicates that the Me31B N-ter motif, C-ter
340 motif, and the FDF motif-binding motif are needed for Me31B's appropriate aggregation
341 status. Furthermore, the three mutant proteins each showed distinct
342 localization/distribution patterns. Me31B$^{N\text{-}ter}$-GFP proteins are found in the nurse cell

343 nucleus (Figure 6A, second row), which is further confirmed by co-staining the egg
344 chambers with DNA stain DAPI (Supplementary Figure 3). Although a small number of
345 Me31B$^{C\text{-}ter}$-GFP aggregates were observed (Figure 6A, third row), they are fewer and
346 smaller than Me31B^{WT}-GFP aggregates. From these observations, we conclude that
347 Me31B's proper aggregation into germline RNP granules requires the presence of both
348 the N-ter motif and the C-ter motif. Previous studies suggest that the two motifs contain
349 different sequence components and, therefore, different potential functions. The N-ter
350 motif contains several ATPase/helicase motifs, including the DEAD-box motif and
351 DVLAAAA motif but no known protein-binding motifs [30-32, 35]; the C-ter motif
352 contains several protein-binding motifs and one putative helicase motif, HRIGR) [10, 19,
353 30, 33, 35, 58]. This means that Me31B likely uses its RNA-interaction ability on both N-
354 ter and C-ter motifs and the protein-binding ability on the C-ter motif to aggregate into
355 the RNP granules. In line with this speculation, the failure of Me31B^{FDF}-GFP to
356 aggregate (Figure 6A, bottom row) suggests binding and recruitment by FDF-motif
357 proteins like Tral and EDC3 [34, 60] is necessary for the aggregation process. Another
358 protein-aggregation factor in Me31B worth noting is the two predicted Intrinsically
359 Disordered Regions (IDRs) at the N-ter end (AA 1- 53) and the C-ter ends (AA 431 –
360 459). Deleting the IDRs was demonstrated to cause rapid self-assembly of Me31B into
361 aggregate-like structures *in vitro*, so the IDRs were suggested to attenuate the
362 interactions between the folded N-ter and C-ter motifs [61]. The above evidence shows
363 that Me31B aggregation to germline RNP granule could be a complex interplay between
364 RNA-interacting, partner protein binding, and IDRs.

365 About the confounding nuclear localization of Me31B$^{N\text{-}ter}$ proteins, we speculate that
366 Me31B may be a nucleocytoplasmic shuttling protein with a Nuclear Localization Signal
367 (NLS) sequence in the N-terminal motif. This NLS sequence leads Me31B into the
368 nucleus, and then the C-terminal motif mediates the protein's export and retention in the
369 cytoplasm. This speculation is conceptually supported by the nucleocytoplasmic
370 shuttling activities of DDX6 (human homolog of Me31B) [58] and Xp54 (*Xenopus*
371 homolog) [11] in cell culture models. However, our efforts to identify a Nuclear
372 Localization Signal (NLS) sequence by using prediction tools (NLStradamus [62], cNLS
373 Mapper [63], and SeqNLS Prediction Server [64]) were unsuccessful. Although we were
374 able to locate amino acid sequences in Me31B (KSKLKLPPKDNRFK and
375 CIPVLEQIDP) that are homologous to the putative NLS and Nuclear Export Signals
376 (NES) sequences in DDX6 [58], respectively, experimental evidence is still needed to
377 validate their *in vivo* functionality. We do not exclude the possibility that the N-terminal
378 NLS is just a non-functional sequence normally masked in folded, full-length Me31B
379 protein. The sequence was accidentally exposed to nucleus transportation machinery
380 upon the deletion of the C-terminal motif.

381 In the early-to-mid stage egg chambers (Figure 6B), we observed that Me31B
382 enrichment in developing oocytes is abolished in the three mutants. In the *me31B^{WT}*
383 control egg chambers, Me31B^{WT}-GFP and Tral were highly enriched in the developing
384 oocytes, with the two proteins extensively overlapping (Figure 6B, first row). However, in
385 the *me31B$^{N\text{-}ter}$* and *me31B$^{C\text{-}ter}$* egg chambers, the mutant Me31B proteins show no
386 pronounced enrichment in the future oocytes (Figure 6B, second and third row), while
387 Tral's enrichment pattern remains unaffected. In the *me31B^{FDF}* mutants, the Me31B^{FDF}-

388 GFP proteins still showed enrichment in the oocytes, but it is much weaker than the
389 Me31B^{WT}-GFP control. We conclude that the Me31B N-ter motif, C-ter motif, and the
390 FDF motif-binding motif are needed for the protein's proper accumulation into future
391 oocytes at early-to-mid stages. For similar reasons discussed before, we suggest that
392 Me31B's transport/accumulation into the oocytes depends on its RNA interaction and
393 protein-binding abilities. This speculation is in line with the observation that Me31B^{FDF}
394 proteins maintained a reduced enrichment in the oocytes: the protein's intact RNA-
395 interacting motifs or other protein-binding motifs could have enabled ineffective but
396 functional transportation into the oocytes.

397 In the mid-stage egg chambers (Figure 6C), Me31B^{WT} proteins were found along the
398 cortex and localized to the germ plasm area of the oocytes (Figure 6C, first row), similar
399 to the Me31B proteins in wildtype strains as previously reported [28]. In the *me31B$^{N\text{-}ter}$*,
400 *me31B$^{C\text{-}ter}$*, and *me31B^{FDF}* mutants, the three mutant proteins localized to the above
401 areas, but the localized proteins appeared to have less granularity (Figure 6C, bottom
402 three rows), consistent with the diffused status of the mutant proteins in earlier stages.

403 All in all, this study took a mutagenesis approach to investigate the *in vivo* functions of
404 six key motifs of DEAD-box RNA helicase Me31B, and the results are summarized in
405 Figure 7. The three ATPase/helicase motifs (DEAD-box, DVLARAK, and HRIGR) are
406 conserved among the members of the Me31B protein family, and mutations in each of
407 them result in alleles (*me31B^{E208A}*, *me31B^{DVLAAAA}*, and *me31B^{R385Q}*) that cause
408 dominant female sterility. Their sterility exhibits oogenesis defects like nurse cell
409 dumping defects, egg chamber degeneration, and early embryogenesis arrest
410 accompanied by embryo morphological abnormalities. In our attempt to find the

411 molecular-level mechanism by which the ATPase/helicase motif mutations cause
412 sterility, we analyzed the *me31B*^{DVLAAAA} heterozygous mutant and showed that the
413 mutation altered *nos* mRNA localization in the germ plasm and decreased *nos* and *osk*
414 transcript levels, highlighting Me31B ATPase/helicase's function in maintaining germline
415 mRNA localization and transcript level. Our additional analysis of Me31B's N-ter motif,
416 C-ter motif, and FDF motif-binding motif demonstrated their impotence in fertility,
417 maintaining Me31B protein level and aggregation status, and subcellular localization.
418 The results from this study provided insight into the molecular mechanisms of key
419 functional motifs in *Drosophila* Me31B. Considering the conserved nature of Me31B and
420 its homologs, these data aid in paving the road to understanding the functions and
421 important regions of Me31B family proteins in various cell types and across different
422 species.
423

424 Materials and Methods

425 Fly strain generation by CRISPR gene editing

426 Mutant *me31B Drosophila* strains were generated using the previously reported
427 CRISPR procedure [65, 66]. Specifically, CRISPR Optimal Target Finder [65] and
428 DRSC/TRiP Functional Genomics Resources (Harvard Medical School) were used to
429 find gRNA cutting sites flanking the *me31B* gene in the *Drosophila* genome. Then, the
430 found gRNA sequences were cloned into gRNA-expressing plasmid vector pCFD5
431 (Addgene) according to a previously published protocol [67]. According to suggested
432 protocols, HDR donor plasmids carrying wild type *me31B* gene were constructed by
433 cloning *me31B* gene DNA into the pHD-sfGFP-ScarlessDsRed cloning vector

434 (Addgene). In the constructed HDR plasmids, the super-fold GFP (*sfGFP*) gene is
435 positioned in-frame and downstream of the *me31B* gene so that the sfGFP protein is
436 tagged to the C-terminal end of the expressed Me31B proteins. The *DsRed* marker
437 gene is positioned in the intergenic region downstream of the *me31B* gene. HDR
438 plasmid with mutant *me31B* genes was generated by mutating the *me31B* wild-type
439 gene in the wild type HDR donor plasmid using the Site-Directed Mutagenesis kit (New
440 England Biolabs) according to the manufacturer's recommended protocols. The
441 resulting HDR plasmids containing different *me31B* alleles are named after the
442 mutations (Figure 1). The gRNA-expressing plasmid and the HDR donor plasmids were
443 co-injected into the Cas9-expressing strain (Genetivision) to generate desired wild-type
444 and *mutant* me31B strains, which were crossed with a second chromosome balancer to
445 establish balanced stocks when possible. The plasmid vectors constructed and the
446 obtained *me31B* strains were validated by sequencing.

447 **Genetic crosses**

448 Balanced *me31B* wild type and mutant strains were self-crossed to obtain homozygous
449 mutant strains. For the dominant female sterile *me31B* strains, males carrying the
450 mutant allele were crossed with w^{1118} (Bloomington Drosophila Stock Center 3605)
451 females to obtain heterozygous strains.

452 **Immunohistochemistry**

453 *Drosophila* ovary immunostaining was performed as previously described [24, 68, 69].
454 The following antibody dilutions were used: Rabbit-anti-Tral (1:1,000). Donkey-anti-
455 Rabbit-Cy3 secondary antibodies (Jackson ImmunoResearch) were used at 1:500.
456 Images were captured by an Olympus FV3000 confocal laser scanning microscope.

457 **Western blots**

458 Western blot antibodies were used at the following dilutions: rabbit-anti-GFP
459 (1:100,000), and mouse-anti-α-Tubulin (1:100,000). Secondary antibodies were used at
460 the following dilutions: mouse-anti-rabbit HRP (Jackson ImmunoResearch) (1:10,000 for
461 rabbit-anti-GFP), goat-anti-mouse HRP (Santa Cruz Biotechnology) (1: 50,000 for
462 mouse-anti-α-Tubulin primary antibody). The protein band quantification analysis was
463 performed by using ImageJ (https://imagej.nih.gov/ij/)

464 **Fertility assay (for *me31B^{WT}*, *me31B$^{N\text{-}ter}$*, *me31B$^{C\text{-}ter}$*, and *me31B^{FDF}* strains)**

465 Fertility assays were performed according to previously established protocols [59].
466 Briefly, virgin females from *me31B^{WT}*, *me31B$^{N\text{-}ter}$*, *me31B$^{C\text{-}ter}$*, and *me31B^{FDF}* strains
467 were collected and allowed to age for 3 – 4 days separately in fly food vials. Each
468 female was then put in a vial with a *w^{1118}* male. After 24 hours, the males were removed
469 from the vials, and the fertilized females were transferred to a new vial every day for the
470 next ten days. The eggs laid and the progenies hatched from each vial were counted.
471 The hatch rate of each vial is calculated by dividing the progenies hatched by the
472 number of eggs laid. An equal amount (15 ml) of fly food medium (Molasses
473 Formulation, Genesee Scientific) was used in each vial.

474 **Number of egg laying, embryo morphology, and embryo hatchability (*me31B^{E208A}*,**
475 ***me31B^{DVLAAAA}*, and *me31B^{R385Q}* strains)**

476 To record the number of eggs laid from the *me31B^{DVLAAAA}*/+ strain, 40 females from the
477 strain were put into a small embryo collection cage with grape-agar plates
478 (Genetivision) in the presence of 10 *w^{1118}* males. After letting the flies adjust for 24
479 hours, the flies were given a fresh grape agar plate, and the eggs laid in the next 24

480 hours were counted. Control experiments were conducted with w^{1118} females, and six
481 independent replicates were performed. To observe the morphology and the hatchability
482 of the embryos from *me31B*^{E208A}/+, *me31B*^{DVLAAAA}/+, *me31B*^{R385Q}/+, and w^{1118} control
483 strains, approximately 80 females from each strain were put into a small embryo
484 collection cage in the presence of 20 w^{1118} males. The embryos were collected on grape
485 agar plates at 25ºC after 24 hours. The embryos were counted and analyzed under a
486 dissection microscope for their morphology. The embryos' hatchability was calculated
487 by counting the number of embryos that failed to develop to later stages 72 hours after
488 the eggs were laid and subtracting this number from the total number of eggs laid.

489 **RNA extraction, cDNA synthesis, and quantitative RT-PCR**

490 According to the manufacturer's instructions, total ovarian RNA was extracted from 5 µl
491 freshly dissected fly ovaries using Qiagen RNeasy Purification Kit (Qiagen). The
492 obtained RNA samples' concentrations were measured by using NanoDrop 2000c. The
493 RNAs were reversely transcribed to cDNAs using the High-Capacity cDNA Reverse
494 Transcription Kit (ThermoFisher) according to the manufacturer's instructions. The
495 synthesized cDNAs were then used for quantitative PCR using Luna Universal qPCR
496 Master Mix (New England Biolabs). The following PCR Primers were used in this study:
497 *nos* forward 5' GTCACCAGCAAACGGACGAGATT -3', *nos* reverse
498 CGGAGCACTCCCGTAGGACAT, *osk* forward 5'- TTGCTGAGCCACGCCCAGAA -3',
499 *osk* reverse 5'- ACATTGGGAATGGTCAGCAGGAAATC -3', *rp49* forward 5'-
500 GCTAAGCTGTCGCACAAA, *rp49* reverse 5'- TCCGGTGGGCAGCATGTG -3'. *rp49*
501 RNA was used as the reference. Data analysis was conducted by using the CFX
502 Manager Software (BioRad) and Microsoft Excel.

503 **smFISH, image analysis, and computational modeling**

504 smFISH was carried out as previously described using published *nos* probe sequences
505 [56, 57, 70]. In summary, ovaries were dissected from yeast-fed females in cold PBS in
506 under 10 minutes, and tissues were fixed for 30 minutes in 4% paraformaldehyde and
507 PBS solution. Tissue was incubated with smFISH probes overnight at 37 ºC in the
508 hybridization solution previously described [56]. For imaging, egg chambers were
509 mounted in Prolong Glass (Life Technologies) and were allowed to cure for 72 hours at
510 room temperature [56, 57]. A Leica STELLARIS 5 confocal microscope was used for
511 imaging *nos* smFISH experiments described in detail [57]. The identification and
512 quantification of unlocalized single *nos* transcripts and localized *nos* homotypic clusters
513 were carried out using a custom MATLAB (Mathworks) program described and
514 published [56, 57]. Confocal images shown in Figure 3 are maximum projections that
515 were filtered by a balanced circular difference-of-Gaussian with a center radius size of
516 1.2 pixels and surround size of 2.2 pixels as previously done for other germ plasm
517 studies [55, 57]. The total number of homotypic clusters identified is reported in the
518 figure legends. For modeling experiments, we employed a previously published model
519 that simulates the formation of germ granules, including *nos* homotypic clusters [57].
520 The only modeling parameters that were adjusted were 1) carrying capacity, which is
521 regulated by Osk levels, was set from 1 (wild type) to 0.56, and 2) the pool of *nos*
522 transcript expression was set from 1 (wild type) to 0.61 to mimic the RT-PCR levels
523 reported in our results section [57].

524 **Statistical Analysis**

525 Reported p-values between average *nos* homotypic cluster sizes were performed using
526 an ANOVA test with a post-hoc Tukey test that was calculated using R statistical
527 programming and R Studio using the function aov and TukeyHSD functions [71, 72].
528 Violin plots were created using the ggplot and ggstatsplot packages [73, 74].

529 Acknowledgments

530 We thank the members of the Gao Lab for discussing and revising this manuscript. We
531 thank Dr. Olivia Rissland and Dr. Akira Nakamura for their kind gifts of antibodies. We
532 thank the Center for Biological Imaging at Kean University for assisting with image
533 acquisition and the members and the Niepielko Lab for their helpful comments and
534 fruitful discussions. Research reported in this publication was supported by the Eunice
535 Kennedy Shriver National Institute of Child Health & Human Development of the
536 National Institutes of Health under award no. R15HD102960 to MGN and
537 1R15HD092925-01A1 to MG.

538 Author Contributions

539 MG conceived and directed the project. MG and MGN wrote the manuscript with input
540 from all authors. EK, MP, IF, and NM performed the fertility assays. AM, CD, and JE
541 generated the CRISPR strains. MGN, DAD, and BMO performed the microscopic
542 analysis, smFISH experiments, and modeling. KAS and YM performed the confocal
543 microscopy experiments. BP, ARM, and DG performed the Western blots and data
544 analysis. All authors discussed the results and commented on the manuscript.

545 Competing Interests

546 The authors declare no competing interests.

547 **Data Availability**

548 All the data presented in this study are included in this manuscript or its
549 supplementary information.

550 **References**

551 1. Nakamura, A., Amikura, R., Hanyu, K. & Kobayashi, S. (2001) Me31B silences
552 translation of oocyte-localizing RNAs through the formation of cytoplasmic RNP
553 complex during Drosophila oogenesis, *Development.* **128**, 3233-42.
554 2. Wang, M., Ly, M., Lugowski, A., Laver, J. D., Lipshitz, H. D., Smibert, C. A. &
555 Rissland, O. S. (2017) ME31B globally represses maternal mRNAs by two distinct
556 mechanisms during the Drosophila maternal-to-zygotic transition, *Elife.* **6**.
557 3. Gotze, M., Dufourt, J., Ihling, C., Rammelt, C., Pierson, S., Sambrani, N., Temme,
558 C., Sinz, A., Simonelig, M. & Wahle, E. (2017) Translational repression of the
559 Drosophila nanos mRNA involves the RNA helicase Belle and RNA coating by Me31B
560 and Trailer hitch, *RNA*.
561 4. Kugler, J. M., Chicoine, J. & Lasko, P. (2009) Bicaudal-C associates with a Trailer
562 Hitch/Me31B complex and is required for efficient Gurken secretion, *Dev Biol.* **328**, 160-
563 72.
564 5. Liu, L., Qi, H., Wang, J. & Lin, H. (2011) PAPI, a novel TUDOR-domain protein,
565 complexes with AGO3, ME31B and TRAL in the nuage to silence transposition,
566 *Development.* **138**, 1863-73.

567 6. Langerak, S., Trombley, A., Patterson, J. R., Leroux, D., Couch, A., Wood, M. P. &
568 Schisa, J. A. (2019) Remodeling of the endoplasmic reticulum in Caenorhabditis
569 elegans oocytes is regulated by CGH-1, *Genesis.* **57**, e23267.
570 7. Ko, S., Kawasaki, I. & Shim, Y. H. (2013) PAB-1, a Caenorhabditis elegans poly(A)-
571 binding protein, regulates mRNA metabolism in germline by interacting with CGH-1 and
572 CAR-1, *PLoS One.* **8**, e84798.
573 8. Kashima, M., Kumagai, N., Agata, K. & Shibata, N. (2016) Heterogeneity of
574 chromatoid bodies in adult pluripotent stem cells of planarian Dugesia japonica, *Dev*
575 *Growth Differ.* **58**, 225-37.
576 9. Yoshida-Kashikawa, M., Shibata, N., Takechi, K. & Agata, K. (2007) DjCBC-1, a
577 conserved DEAD box RNA helicase of the RCK/p54/Me31B family, is a component of
578 RNA-protein complexes in planarian stem cells and neurons, *Dev Dyn.* **236**, 3436-50.
579 10. Alves-Rodrigues, I., Mas, A. & Diez, J. (2007) Xenopus Xp54 and human RCK/p54
580 helicases functionally replace yeast Dhh1p in brome mosaic virus RNA replication, *J*
581 *Virol.* **81**, 4378-80.
582 11. Smillie, D. A. & Sommerville, J. (2002) RNA helicase p54 (DDX6) is a shuttling
583 protein involved in nuclear assembly of stored mRNP particles, *J Cell Sci.* **115**, 395-407.
584 12. Aravin, A. A., van der Heijden, G. W., Castaneda, J., Vagin, V. V., Hannon, G. J. &
585 Bortvin, A. (2009) Cytoplasmic compartmentalization of the fetal piRNA pathway in
586 mice, *PLoS Genet.* **5**, e1000764.
587 13. Swetloff, A., Conne, B., Huarte, J., Pitetti, J. L., Nef, S. & Vassalli, J. D. (2009)
588 Dcp1-bodies in mouse oocytes, *Mol Biol Cell.* **20**, 4951-61.

589 14. Lin, F., Wang, R., Shen, J. J., Wang, X., Gao, P., Dong, K. & Zhang, H. Z. (2008)
590 Knockdown of RCK/p54 expression by RNAi inhibits proliferation of human colorectal
591 cancer cells in vitro and in vivo, *Cancer Biol Ther.* **7**, 1669-76.
592 15. Marcon, B. H., Rebelatto, C. K., Cofre, A. R., Dallagiovanna, B. & Correa, A. (2020)
593 DDX6 Helicase Behavior and Protein Partners in Human Adipose Tissue-Derived Stem
594 Cells during Early Adipogenesis and Osteogenesis, *Int J Mol Sci.* **21**.
595 16. Wang, Y., Arribas-Layton, M., Chen, Y., Lykke-Andersen, J. & Sen, G. L. (2015)
596 DDX6 Orchestrates Mammalian Progenitor Function through the mRNA Degradation
597 and Translation Pathways, *Mol Cell.* **60**, 118-30.
598 17. Hansen, M., Zeddies, S., Meinders, M., di Summa, F., van Alphen, F. P. J.,
599 Hoogendijk, A. J., Moore, K. S., Halbach, M., Gutierrez, L., van den Biggelaar, M.,
600 Thijssen-Timmer, D. C., Auburger, G. W. J., van den Akker, E., von Lindern, M. &
601 Rollmann, E. (2020) The RNA-Binding Protein ATXN2 is Expressed during
602 Megakaryopoiesis and May Control Timing of Gene Expression, *Int J Mol Sci.* **21**.
603 18. Di Stefano, B., Luo, E. C., Haggerty, C., Aigner, S., Charlton, J., Brumbaugh, J., Ji,
604 F., Rabano Jimenez, I., Clowers, K. J., Huebner, A. J., Clement, K., Lipchina, I., de Kort,
605 M. A. C., Anselmo, A., Pulice, J., Gerli, M. F. M., Gu, H., Gygi, S. P., Sadreyev, R. I.,
606 Meissner, A., Yeo, G. W. & Hochedlinger, K. (2019) The RNA Helicase DDX6 Controls
607 Cellular Plasticity by Modulating P-Body Homeostasis, *Cell Stem Cell.* **25**, 622-638 e13.
608 19. Weston, A. & Sommerville, J. (2006) Xp54 and related (DDX6-like) RNA helicases:
609 roles in messenger RNP assembly, translation regulation and RNA degradation, *Nucleic*
610 *Acids Res.* **34**, 3082-94.

611 20. Chu, C. Y. & Rana, T. M. (2006) Translation repression in human cells by
612 microRNA-induced gene silencing requires RCK/p54, *PLoS Biol.* **4**, e210.
613 21. Barckmann, B., Pierson, S., Dufourt, J., Papin, C., Armenise, C., Port, F.,
614 Grentzinger, T., Chambeyron, S., Baronian, G., Desvignes, J. P., Curk, T. & Simonelig,
615 M. (2015) Aubergine iCLIP Reveals piRNA-Dependent Decay of mRNAs Involved in
616 Germ Cell Development in the Early Embryo, *Cell Rep.* **12**, 1205-16.
617 22. Jeske, M., Moritz, B., Anders, A. & Wahle, E. (2011) Smaug assembles an ATP-
618 dependent stable complex repressing nanos mRNA translation at multiple levels, *EMBO*
619 *J.* **30**, 90-103.
620 23. Sudhakaran, I. P., Hillebrand, J., Dervan, A., Das, S., Holohan, E. E., Hulsmeier, J.,
621 Sarov, M., Parker, R., VijayRaghavan, K. & Ramaswami, M. (2014) FMRP and Ataxin-2
622 function together in long-term olfactory habituation and neuronal translational control,
623 *Proc Natl Acad Sci U S A.* **111**, E99-E108.
624 24. DeHaan, H., McCambridge, A., Armstrong, B., Cruse, C., Solanki, D., Trinidad, J.
625 C., Arkov, A. L. & Gao, M. (2017) An in vivo Proteomic Analysis of the Me31B
626 Interactome in Drosophila Germ Granules, *FEBS Lett*.
627 25. Arkov, A. L. & Ramos, A. (2010) Building RNA-protein granules: insight from the
628 germline, *Trends Cell Biol.* **20**, 482-90.
629 26. Voronina, E., Seydoux, G., Sassone-Corsi, P. & Nagamori, I. (2011) RNA granules
630 in germ cells, *Cold Spring Harb Perspect Biol.* **3**.
631 27. Rangan, P., DeGennaro, M., Jaime-Bustamante, K., Coux, R. X., Martinho, R. G. &
632 Lehmann, R. (2009) Temporal and spatial control of germ-plasm RNAs, *Curr Biol.* **19**,
633 72-7.

634 28. McCambridge, A., Solanki, D., Olchawa, N., Govani, N., Trinidad, J. C. & Gao, M.
635 (2020) Comparative Proteomics Reveal Me31B's Interactome Dynamics, Expression
636 Regulation, and Assembly Mechanism into Germ Granules during Drosophila Germline
637 Development, *Sci Rep.* **10**, 564.
638 29. Sankaranarayanan, M., Emenecker, R. J., Jahnel, M., Trussina, I. R. E. A.,
639 Wayland, M., Alberti, S., Holehouse, A. S. & Weil, T. T. (2021) The arrested state of
640 processing bodies supports mRNA regulation in early development, *bioRxiv*,
641 2021.03.16.435709.
642 30. Minshall, N., Kress, M., Weil, D. & Standart, N. (2009) Role of p54 RNA helicase
643 activity and its C-terminal domain in translational repression, P-body localization and
644 assembly, *Mol Biol Cell.* **20**, 2464-72.
645 31. Barbee, S. A., Estes, P. S., Cziko, A. M., Hillebrand, J., Luedeman, R. A., Coller, J.
646 M., Johnson, N., Howlett, I. C., Geng, C., Ueda, R., Brand, A. H., Newbury, S. F.,
647 Wilhelm, J. E., Levine, R. B., Nakamura, A., Parker, R. & Ramaswami, M. (2006)
648 Staufen- and FMRP-containing neuronal RNPs are structurally and functionally related
649 to somatic P bodies, *Neuron.* **52**, 997-1009.
650 32. Minshall, N., Thom, G. & Standart, N. (2001) A conserved role of a DEAD box
651 helicase in mRNA masking, *RNA.* **7**, 1728-42.
652 33. Tritschler, F., Eulalio, A., Helms, S., Schmidt, S., Coles, M., Weichenrieder, O.,
653 Izaurralde, E. & Truffault, V. (2008) Similar modes of interaction enable Trailer Hitch
654 and EDC3 to associate with DCP1 and Me31B in distinct protein complexes, *Mol Cell*
655 *Biol.* **28**, 6695-708.

656 34. Tritschler, F., Braun, J. E., Eulalio, A., Truffault, V., Izaurralde, E. & Weichenrieder,
657 O. (2009) Structural basis for the mutually exclusive anchoring of P body components
658 EDC3 and Tral to the DEAD box protein DDX6/Me31B, *Mol Cell.* **33**, 661-8.
659 35. Peter, D., Ruscica, V., Bawankar, P., Weber, R., Helms, S., Valkov, E., Igreja, C. &
660 Izaurralde, E. (2019) Molecular basis for GIGYF-Me31B complex assembly in 4EHP-
661 mediated translational repression, *Genes Dev.* **33**, 1355-1360.
662 36. Hara, M., Lourido, S., Petrova, B., Lou, H. J., Von Stetina, J. R., Kashevsky, H.,
663 Turk, B. E. & Orr-Weaver, T. L. (2018) Identification of PNG kinase substrates uncovers
664 interactions with the translational repressor TRAL in the oocyte-to-embryo transition,
665 *Elife.* **7**.
666 37. Cheng, Z., Coller, J., Parker, R. & Song, H. (2005) Crystal structure and functional
667 analysis of DEAD-box protein Dhh1p, *RNA.* **11**, 1258-70.
668 38. Intile, P. J., Balzer, G. J., Wolfgang, M. C. & Yahr, T. L. (2015) The RNA Helicase
669 DeaD Stimulates ExsA Translation To Promote Expression of the Pseudomonas
670 aeruginosa Type III Secretion System, *J Bacteriol.* **197**, 2664-74.
671 39. Liao, S. E., Kandasamy, S. K., Zhu, L. & Fukunaga, R. (2019) DEAD-box RNA
672 helicase Belle posttranscriptionally promotes gene expression in an ATPase activity-
673 dependent manner, *RNA.* **25**, 825-839.
674 40. Mugler, C. F., Hondele, M., Heinrich, S., Sachdev, R., Vallotton, P., Koek, A. Y.,
675 Chan, L. Y. & Weis, K. (2016) ATPase activity of the DEAD-box protein Dhh1 controls
676 processing body formation, *Elife.* **5**.

677 41. Story, R. M., Li, H. & Abelson, J. N. (2001) Crystal structure of a DEAD box protein
678 from the hyperthermophile Methanococcus jannaschii, *Proc Natl Acad Sci U S A.* **98**,
679 1465-70.
680 42. Buszczak, M. & Cooley, L. (2000) Eggs to die for: cell death during Drosophila
681 oogenesis, *Cell Death Differ.* **7**, 1071-4.
682 43. McCall, K. & Steller, H. (1998) Requirement for DCP-1 caspase during Drosophila
683 oogenesis, *Science.* **279**, 230-4.
684 44. Shen, R., Weng, C., Yu, J. & Xie, T. (2009) eIF4A controls germline stem cell self-
685 renewal by directly inhibiting BAM function in the Drosophila ovary, *Proc Natl Acad Sci*
686 *U S A.* **106**, 11623-8.
687 45. Oberer, M., Marintchev, A. & Wagner, G. (2005) Structural basis for the
688 enhancement of eIF4A helicase activity by eIF4G, *Genes Dev.* **19**, 2212-23.
689 46. Pause, A., Methot, N. & Sonenberg, N. (1993) The HRIGRXXR region of the DEAD
690 box RNA helicase eukaryotic translation initiation factor 4A is required for RNA binding
691 and ATP hydrolysis, *Mol Cell Biol.* **13**, 6789-98.
692 47. Pause, A. & Sonenberg, N. (1992) Mutational analysis of a DEAD box RNA
693 helicase: the mammalian translation initiation factor eIF-4A, *EMBO J.* **11**, 2643-54.
694 48. Chen, W., Hu, Y., Lang, C. F., Brown, J. S., Schwabach, S., Song, X., Zhang, Y.,
695 Munro, E., Bennett, K., Zhang, D. & Lee, H. C. (2020) The Dynamics of P Granule
696 Liquid Droplets Are Regulated by the Caenorhabditis elegans Germline RNA Helicase
697 GLH-1 via Its ATP Hydrolysis Cycle, *Genetics.* **215**, 421-434.

698 49. Marnik, E. A., Fuqua, J. H., Sharp, C. S., Rochester, J. D., Xu, E. L., Holbrook, S.
699 E. & Updike, D. L. (2019) Germline Maintenance Through the Multifaceted Activities of
700 GLH/Vasa in Caenorhabditis elegans P Granules, *Genetics.* **213**, 923-939.
701 50. Lehmann, R. (2016) Germ Plasm Biogenesis--An Oskar-Centric Perspective, *Curr*
702 *Top Dev Biol.* **116**, 679-707.
703 51. Gao, M. & Arkov, A. L. (2013) Next generation organelles: structure and role of
704 germ granules in the germline, *Mol Reprod Dev.* **80**, 610-23.
705 52. Jamieson-Lucy, A. & Mullins, M. C. (2019) The vertebrate Balbiani body, germ
706 plasm, and oocyte polarity, *Curr Top Dev Biol.* **135**, 1-34.
707 53. Bilinski, S. M., Jaglarz, M. K. & Tworzydlo, W. (2017) The Pole (Germ) Plasm in
708 Insect Oocytes, *Results Probl Cell Differ.* **63**, 103-126.
709 54. Wang, J. T. & Seydoux, G. (2013) Germ cell specification, *Adv Exp Med Biol.* **757**,
710 17-39.
711 55. Little, S. C., Sinsimer, K. S., Lee, J. J., Wieschaus, E. F. & Gavis, E. R. (2015)
712 Independent and coordinate trafficking of single Drosophila germ plasm mRNAs, *Nat*
713 *Cell Biol.* **17**, 558-68.
714 56. Niepielko, M. G., Eagle, W. V. I. & Gavis, E. R. (2018) Stochastic Seeding Coupled
715 with mRNA Self-Recruitment Generates Heterogeneous Drosophila Germ Granules,
716 *Curr Biol.* **28**, 1872-1881 e3.
717 57. Valentino, M., Ortega, B. M., Ulrich, B., Doyle, D. A., Farnum, E. D., Joiner, D. A.,
718 Gavis, E. R. & Niepielko, M. G. (2022) Computational modeling offers new insight into
719 Drosophila germ granule development, *Biophys J.* **121**, 1465-1482.

720 58. Huang, J. H., Ku, W. C., Chen, Y. C., Chang, Y. L. & Chu, C. Y. (2017) Dual
721 mechanisms regulate the nucleocytoplasmic localization of human DDX6, *Sci Rep.* **7**,
722 42853.
723 59. Mossman, J. A., Mabeza, R. M. S., Blake, E., Mehta, N. & Rand, D. M. (2019) Age
724 of Both Parents Influences Reproduction and Egg Dumping Behavior in Drosophila
725 melanogaster, *J Hered.* **110**, 300-309.
726 60. Tritschler, F., Eulalio, A., Truffault, V., Hartmann, M. D., Helms, S., Schmidt, S.,
727 Coles, M., Izaurralde, E. & Weichenrieder, O. (2007) A divergent Sm fold in EDC3
728 proteins mediates DCP1 binding and P-body targeting, *Mol Cell Biol.* **27**, 8600-11.
729 61. Sankaranarayanan, M., Emenecker, R. J., Wilby, E. L., Jahnel, M., Trussina, I.,
730 Wayland, M., Alberti, S., Holehouse, A. S. & Weil, T. T. (2021) Adaptable P body
731 physical states differentially regulate bicoid mRNA storage during early Drosophila
732 development, *Dev Cell.* **56**, 2886-2901 e6.
733 62. Nguyen Ba, A. N., Pogoutse, A., Provart, N. & Moses, A. M. (2009) NLStradamus:
734 a simple Hidden Markov Model for nuclear localization signal prediction, *BMC*
735 *Bioinformatics.* **10**, 202.
736 63. Kosugi, S., Hasebe, M., Tomita, M. & Yanagawa, H. (2009) Systematic
737 identification of cell cycle-dependent yeast nucleocytoplasmic shuttling proteins by
738 prediction of composite motifs, *Proc Natl Acad Sci U S A.* **106**, 10171-6.
739 64. Lin, J. R. & Hu, J. (2013) SeqNLS: nuclear localization signal prediction based on
740 frequent pattern mining and linear motif scoring, *PLoS One.* **8**, e76864.
741 65. Gratz, S. J., Ukken, F. P., Rubinstein, C. D., Thiede, G., Donohue, L. K.,
742 Cummings, A. M. & O'Connor-Giles, K. M. (2014) Highly specific and efficient

743 CRISPR/Cas9-catalyzed homology-directed repair in Drosophila, *Genetics.* **196**, 961-
744 71.
745 66. Gratz, S. J., Rubinstein, C. D., Harrison, M. M., Wildonger, J. & O'Connor-Giles, K.
746 M. (2015) CRISPR-Cas9 Genome Editing in Drosophila, *Curr Protoc Mol Biol.* **111**, 31 2
747 1-20.
748 67. Port, F. & Bullock, S. L. (2016) Augmenting CRISPR applications in Drosophila with
749 tRNA-flanked sgRNAs, *Nat Methods.* **13**, 852-4.
750 68. Creed, T. M., Loganathan, S. N., Varonin, D., Jackson, C. A. & Arkov, A. L. (2010)
751 Novel role of specific Tudor domains in Tudor-Aubergine protein complex assembly and
752 distribution during Drosophila oogenesis, *Biochem Biophys Res Commun.* **402**, 384-9.
753 69. Arkov, A. L., Wang, J. Y., Ramos, A. & Lehmann, R. (2006) The role of Tudor
754 domains in germline development and polar granule architecture, *Development.* **133**,
755 4053-62.
756 70. Eagle, W. V. I., Yeboah-Kordieh, D. K., Niepielko, M. G. & Gavis, E. R. (2018)
757 Distinct cis-acting elements mediate targeting and clustering of Drosophila polar granule
758 mRNAs, *Development.* **145**.
759 71. Team, R. (2020) RStudio: Integrated Development Environment for R in, RStudio,
760 PBC., Boston, MA.
761 72. Team, R. C. (2020) R: A Language and Environment for Statistical Computing in, R
762 Foundation for Statistical Computing,
763 73. Wickham, H. (2016) *ggplot2: Elegant Graphics for Data Analysis*, pringer-Verlag
764 New York.

74. Patil, I. (2021) Visualizations with statistical details: The ggstatsplot approach, *Journal of Open Source Software.* **6**, 3167.

768 ## Figure Legends

769 **Figure 1. Diagram of the CRISPR-generated Me31B wild-type and mutant proteins**
770 **in the *Drosophila* strains generated for this study.** The bar shape after each Me31B
771 protein name represents the protein's primary structure with numbers on top of the bars
772 to mark the number of amino acids and their positions in the protein. Green
773 Fluorescence Protein (GFP) tags are expressed at the C-terminal end of the
774 constructed Me31B proteins. The point mutations are as follows: E208A, glutamic acid
775 208 replaced by alanine; R101A, arginine 101 replaced by alanine; K103A, lysine 103
776 replaced by alanine; R385Q, arginine 385 replaced by glutamine; C285A, cysteine 285
777 replaced by alanine; L289A, leucine 289 replaced by alanine; Y273S, tyrosine 273
778 replaced by serine; Y274N, tyrosine 274 replaced by asparagine. Me31B$^{N\text{-}ter}$ protein
779 (deletion of amino acids 277 to 459) contains the first 276 amino acids of the wild-type
780 protein. Me31B$^{C\text{-}ter}$ protein (deletion of amino acids 1 to 276) contains the last 183
781 amino acids of the wild-type protein.
782 *Note that two unintended, missense mutations were detected in the *me31B^{FDF}* strain
783 when sequencing its *me31B* gene. The two mutations (Y273S and Y274N) are outside
784 the FDF motif-binding motif.

785 **Figure 2. Defective embryogenesis and oogenesis with heterozygous *me31B^{E208A}*,**
786 ***me31B^{DVLAAAA}*, and *me31B^{R385Q}* strains. (A)** Embryos laid by *w^{1118}* control females all
787 had normal (100%) dorsal appendages. In contrast, embryos laid by *me31B^{E208A}*/+
788 females had fused (45%), shortened (33%), and normal (22%, not shown) dorsal
789 appendages; embryos laid by *me31B^{DVLAAAA}*/+ females had shortened (33%) or normal
790 (67%, not shown) dorsal appendages; embryos laid by *me31B^{R385Q}*/+ females all had

791 severe morphological defects (100%). **(B)** In 52% of late-stage (stage 14) eggs of
792 *me31B*^{E208A}/+ mutant (right panel), dumping of the nurse cell content into the oocyte
793 was incomplete (see highlighted region with yellow dashed lines), in contrast to the
794 complete dumping of *w*^{1118} control eggs (left panel). DAPI staining of the same eggs
795 was shown at the bottom panels, and nurse cell nuclei-like materials were present in the
796 "un-dumped" region of the *me31B*^{E208A}/+ mutant egg. **(C)** Similar dumpless phenotypes
797 were observed in 78% of *me31B*^{DVLAAAA}/+ mutant's late-stage (stage 14) eggs. The "un-
798 dumped" regions (highlighted with yellow dashed lines) were broader than the
799 *me31B*^{E208A}/+ mutant from (B). Only 22% of the *me31B*^{DVLAAAA}/+ mutant's eggs
800 appeared normal. **(D)** Ovarioles from *w*^{1118} and *me31B*^{R385Q}/+ females were stained by
801 DAPI stain. The ovarioles are oriented so that the early-stage egg chambers are on the
802 left and the later-stage egg chambers are on the right. Early-to-mid stage egg chamber
803 degenerations in *me31B*^{R385Q}/+ mutant (right panel) are indicated by arrows, in contrast
804 to the successfully developed early- and mid-stage egg chambers in the *w*^{1118} control
805 (left panel).

806 **Figure 3. smFISH analysis of *nos* mRNA in *me31B*^{DVLAAAA} heterozygous mutant**
807 **and quantitative RT-PCR analysis of *nos* and *osk* mRNA levels in heterozygous**
808 ***me31B*^{E208A}, *me31B*^{DVLAAAA}, and *me31B*^{R385Q} mutants. (A)** Stage 13 oocytes from
809 *me31B*^{WT} and *me31B*^{DVLAAAA} flies, with *nos* (magenta) mRNAs detected using smFISH.
810 The white solid box indicates the unlocalized single transcripts of *nos* that are found in
811 the bulk cytoplasm (enlarged in the second panel) while the broken yellow box
812 highlights *nos* that has localized to the germ plasm by forming homotypic clusters
813 (enlarged and shown as a heatmap in the third panel). **(B)** The distribution of *nos* cluster

814 size (number of *nos* transcripts calculated within a granule) found in each genotype's
815 germ plasm and the computational model. Total clusters identified and analyzed include
816 3,295 from *me31B*^{DVLAAA}, 5,551 from the computational model, 19,195 *me31B*^{WT}, and
817 19,147 from *yellow white* (*yw*). Of note, only oocytes that did not display a dumpless
818 phenotype were included in this analysis. **(C)** In *me31B*^{DVLAAAA}/+ ovaries, *nos* transcript
819 level is 61% ± 7% of that in the *w*^{1118} control ($p < 0.05$) and *osk* transcript level is 56% ±
820 4% of that in the control ($p < 0.05$). **(D)** In *me31B*^{E208A}/+ ovaries, *nos* transcript level is
821 104% ± 7% of that in the *w*^{1118} control (NS), and *osk* transcript level is 162% ± 12% of
822 that in the control (NS, $p = 0.054$). (E) In *me31B*^{R285Q}/+ ovaries, *nos* transcript level is
823 44% ± 2% of that in the *w*^{1118} control ($p < 0.001$) and *osk* transcript level is 194% ± 12%
824 of that in the control ($p < 0.001$). NS: not significant. Error bars represent the standard
825 error of the mean.

826 **Figure 4. Fertility assays of *me31B*$^{N\text{-}ter}$, *me31B*$^{C\text{-}ter}$, and *me31B*^{FDF} mutants. (A)** A
827 *me31B*^{WT} (control), *me31B*$^{N\text{-}ter}$, *me31B*$^{C\text{-}ter}$, and *me31B*^{FDF} female flies lay an average of
828 117, 68, 29, and 77 eggs, respectively. The egg number of *me31B*$^{N\text{-}ter}$, *me31B*$^{C\text{-}ter}$, and
829 *me31B*^{FDF} mutants are 58% ($p < 0.01$), 25% ($p < 0.001$), and 66% ($p < 0.05$) of the
830 *me31B*^{WT} (control), respectively. **(B)** A *me31B*^{WT} (control), *me31B*$^{N\text{-}ter}$, *me31B*$^{C\text{-}ter}$, and
831 *me31B*^{FDF} female fly produced an average of 106, 47, 0, and 75 progenies, respectively.
832 The progeny number of *me31B*$^{N\text{-}ter}$, *me31B*$^{C\text{-}ter}$ and *me31B*^{FDF} mutants are 44% ($p <$
833 0.001), 0% ($p < 0.0001$), and 71% (NS) respectively. NS: not significant. **(C)** The
834 average egg hatch rates for *me31B*^{WT} (control), *me31B*$^{N\text{-}ter}$, *me31B*$^{C\text{-}ter}$, and *me31B*^{FDF}
835 strains are 90.8%, 68.3%, 0%, and 97.1%, respectively. Compared to *me31B*^{WT}, the
836 hatch rate decreases in *me31B*$^{N\text{-}ter}$ and *me31B*$^{C\text{-}ter}$ mutants are statistically significant

837 but not significant in *me31B*^{FDF}. **(D)** Embryos laid by *me31B*$^{C\text{-}ter}$ flies had fused dorsal
838 appendages (68%) or missing dorsal appendages (32%), in contrast to the normal
839 dorsal appendages (100%) in *me31B*^{WT} (control). Error bars represent the standard
840 error of the mean.

841 **Figure 5. Western blot quantification of Me31B protein level in *me31B*$^{N\text{-}ter}$,**
842 ***me31B*$^{C\text{-}ter}$, and *me31B*^{FDF} mutants. (A)** Anti-GFP Western blots were used to quantify
843 the Me31B^{WT}-GFP, Me31B$^{N\text{-}ter}$-GFP, Me31B$^{C\text{-}ter}$-GFP, and Me31B^{FDF}-GFP proteins in
844 the ovaries of the corresponding fly strains. Anti-Tubulin Western blots were used as
845 loading controls. Me31B$^{N\text{-}ter}$ and Me31B$^{C\text{-}ter}$ proteins' expression levels were
846 conspicuously lower than the Me31B^{WT} control protein, while the Me31B^{FDF} protein level
847 is comparable to the control. The images shown are representative images of multiple
848 biological replicates. The additional, uncropped biological replicate images are
849 presented in Supplementary Figure 2. **(B)** The Me31B$^{N\text{-}ter}$-GFP and Me31B$^{C\text{-}ter}$-GFP
850 protein levels are 40% ($p < 0.01$) and 11% ($p < 0.001$) relative to the Me31B^{WT}-GFP
851 control protein, respectively. The me31B^{FDF}-GFP protein level is 114% relative to the
852 control (NS). Western blot image analysis was performed with ImageJ and protein
853 quantifications were normalized using the alpha-tubulin proteins. NS: not statistically
854 significant. Error bars represent the standard error of the mean.

855 **Figure 6. Mutant Me31B proteins in *me31B*$^{N\text{-}ter}$, *me31B*$^{C\text{-}ter}$, and *me31B*^{FDF} strain**
856 **show altered aggregation and localization in developing egg chambers. (A**) In
857 early-stage egg chambers, mutant Me31B-GFP proteins (green channel) in *me31B*$^{N\text{-}ter}$,
858 *me31B*$^{C\text{-}ter}$, and *me31B*^{FDF} strains are much more diffused in the nurse cell and oocytes,
859 in contrast to the aggregated status of Me31B^{WT} in RNP granules like nuage granules

860 and P-bodies. Furthermore, none of the three mutant proteins overlap with partner
861 protein Tral. Unlike Me31B mutant proteins, Tral (Red channel) localization is not
862 affected in the three mutants. In particular, Me31B$^{N\text{-}ter}$-GFP proteins are present in the
863 nuclei of nurse cells. Me31B$^{C\text{-}ter}$-GFP proteins form fewer numbers and smaller size
864 granules than Me31B^{WT}-GFP, and the Me31B$^{C\text{-}ter}$ granules do not associate with Tral-
865 marked granules. Nurse cell perinuclear regions (nuage) are indicated by arrowheads.
866 Arrows indicate p-body granules marked by Tral. Me31B$^{C\text{-}ter}$-GFP and Me31B^{FDF}-GFP
867 proteins were found in ring-like structures that appear to be ring canals (yellow dashed
868 squares, same for B and C), structures that connect the cytoplasm between nurse cells
869 and oocytes and allow for intracellular transportations. **(B)** In early-to-mid stage egg
870 chambers, mutant Me31B-GFP proteins (green channel) in *me31B$^{N\text{-}ter}$* and *me31B$^{C\text{-}ter}$*
871 strains do not enrich within the developing oocytes like that in the *me31B^{WT}* control.
872 Me31B^{FDF}-GFP protein's enrichment in the developing oocytes is weaker than in the
873 control. Tral's (red channel) enrichment in the oocytes is not affected in the three
874 mutants. Developing oocytes are indicated by arrowheads. **(C)** In mid-stage egg
875 chambers, mutant Me31B-GFP proteins of *me31B$^{N\text{-}ter}$*, *me31B$^{C\text{-}ter}$, and me31B^{FDF}*
876 strains localize to the cortex and the germplasm area at the posterior of oocytes, like the
877 control. However, all three mutant Me31B proteins appear more diffused than the
878 aggregated Me31B^{WT}-GFP proteins in the above areas. Arrowheads indicate the germ-
879 plasm areas. Tral's (Red channel) localization to the cortex and germplasm was not
880 affected in the three mutants.

881 **Figure 7. Summary of the Me31B motif functions.** This study uses a target-motif-
882 mutation approach to investigate six functionally important domains/motifs of *Drosophila*

883 Me31B. Our characterization of the generated *me31B* mutants revealed
884 ATPase/helicase motifs' function in female fertility, oogenesis, and embryogenesis
885 (DVLARARK, DEAD-box, and HRIGR motifs). An in-depth analysis of the DVLARAK
886 motif mutation uncovered its function in maintaining *nos* mRNA localization and the
887 transcript level of *nos* and *osk* mRNA levels. We further showed the Me31B N-terminal
888 motif, C-terminal motif, and FDF motif-binding motif's function in female fertility and their
889 different roles in maintaining the Me31B protein level and subcellular localization.

Figure 1

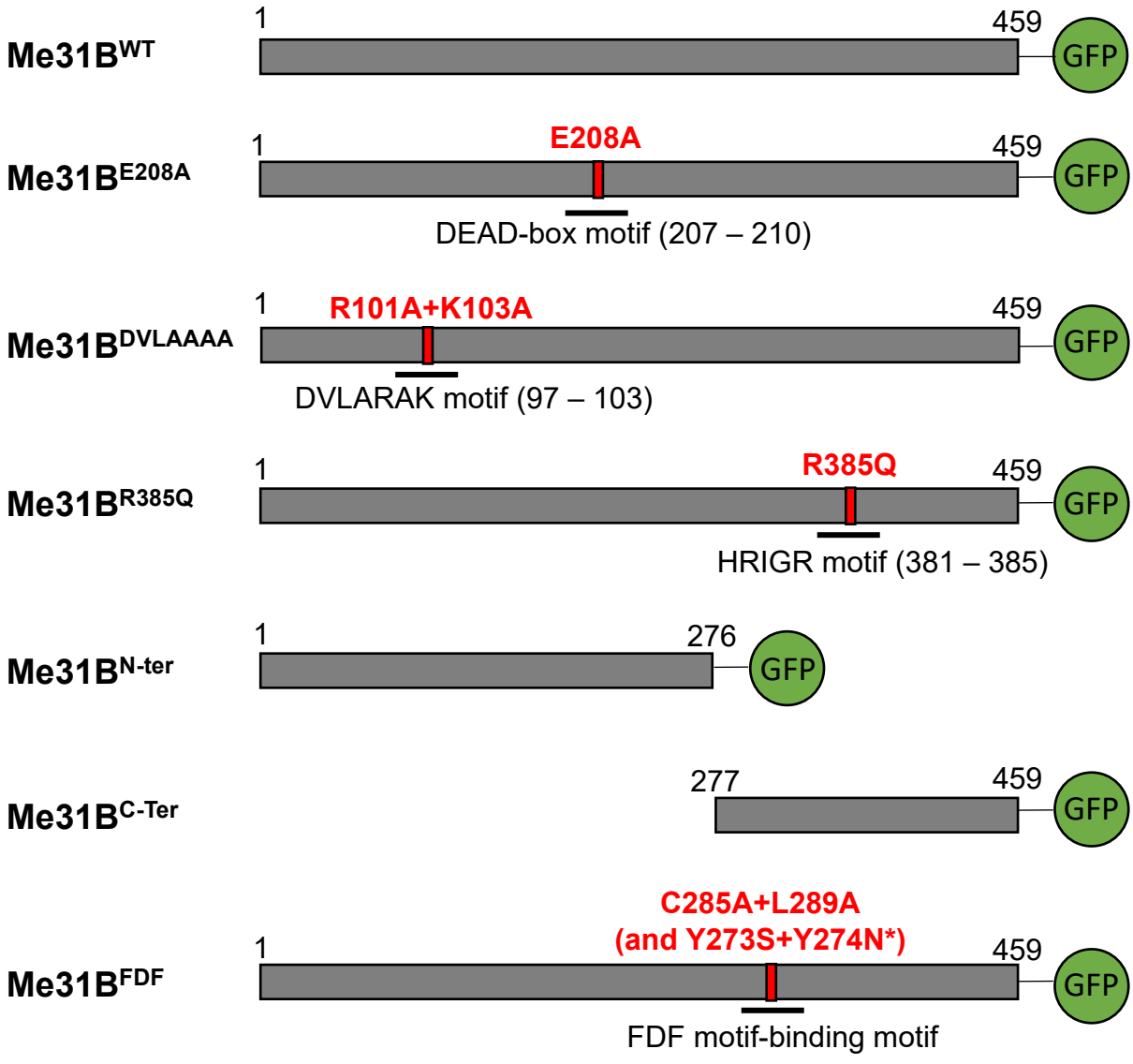
Me31B^WT
1
459
GFP
Me31B^E208A
1
E208A
459
GFP
DEAD-box motif (207 – 210)
Me31B^DVLAAAA
1
R101A+K103A
459
GFP
DVLARAK motif (97 – 103)
Me31B^R385Q
1
R385Q
459
GFP
HRIGR motif (381 – 385)
Me31B^N-ter
1
276
GFP
Me31B^C-Ter
277
459
GFP
Me31B^FDF
1
C285A+L289A
(and Y273S+Y274N*)
459
GFP
FDF motif-binding motif

Figure 2

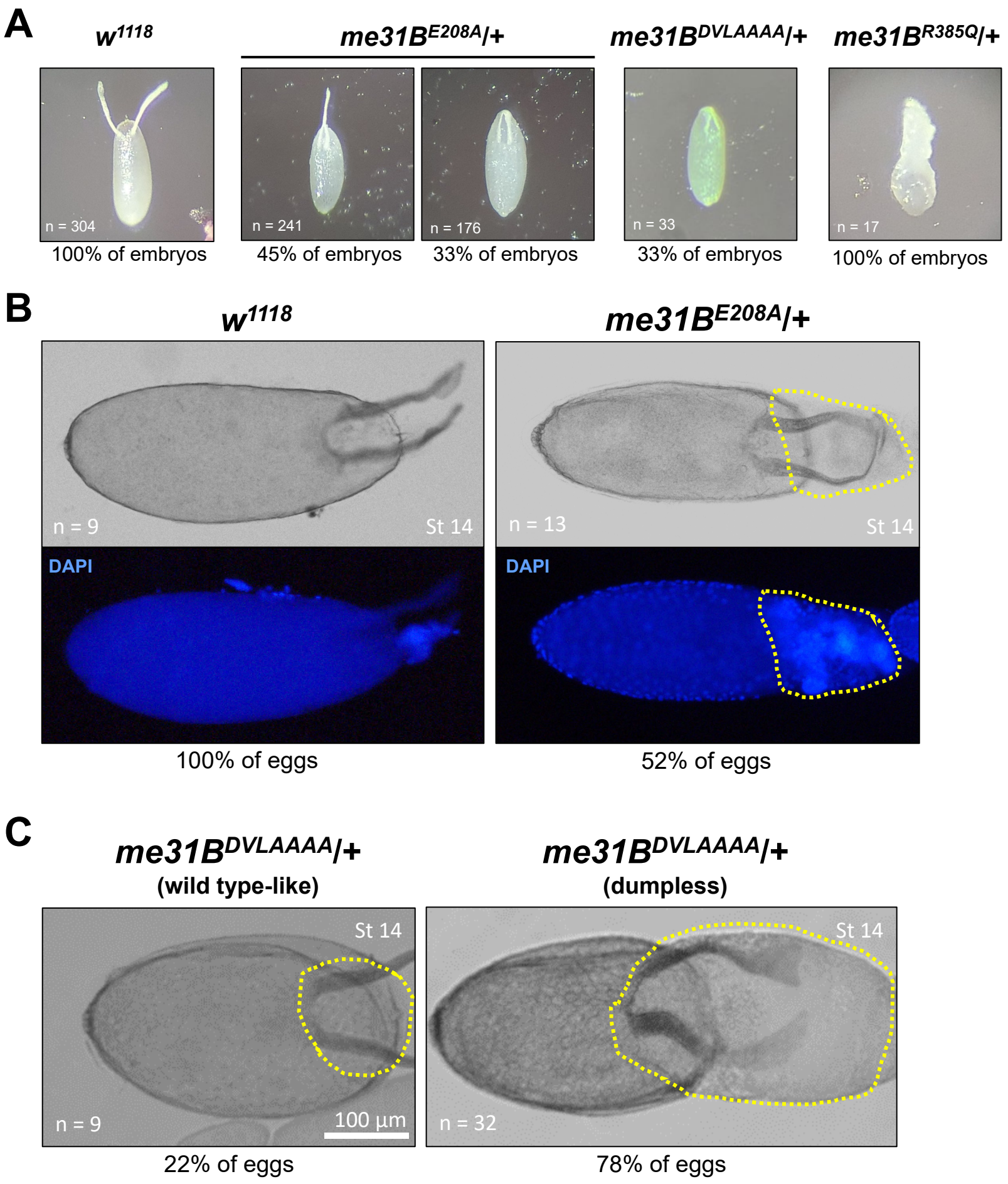
A
w1118
me31BE208A/+
me31BDVLAAAA/+
me31BR385Q/+
n = 304
n = 241
n = 176
n = 33
n = 17
100% of embryos
45% of embryos
33% of embryos
33% of embryos
100% of embryos
B
w1118
me31BE208A/+
n = 9
St 14
n = 13
St 14
DAPI
DAPI
100% of eggs
52% of eggs
C
me31BDVLAAAA/+
(wild type-like)
me31BDVLAAAA/+
(dumpless)
St 14
St 14
n = 9
100 µm
n = 32
22% of eggs
78% of eggs
D
w1118
me31BR385Q/+
DAPI
DAPI
oocyte
n = 35
n = 30

Figure 3

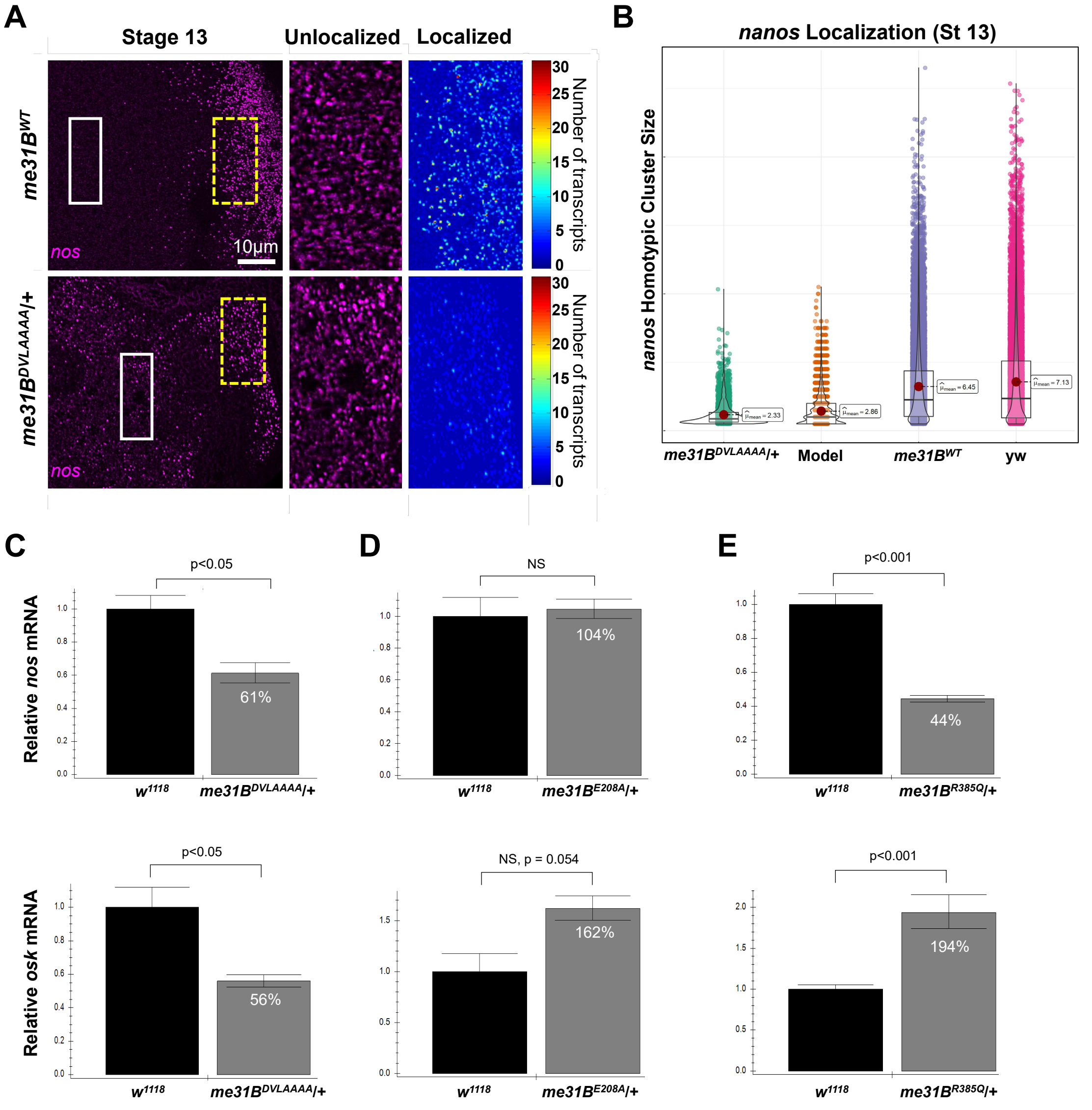
A
Stage 13
Unlocalized
Localized
me31B^WT
me31B^DVLAAAA/+
nos
10µm
Number of transcripts
30
25
20
15
10
5
0
B
nanos Localization (St 13)
nanos Homotypic Cluster Size
me31B^DVLAAAA/+
Model
me31B^WT
yw
μ̂mean = 2.33
μ̂mean = 2.86
μ̂mean = 6.45
μ̂mean = 7.13
C
p<0.05
Relative nos mRNA
61%
w1118
me31B^DVLAAAA/+
D
NS
104%
me31B^E208A/+
E
p<0.001
44%
me31B^R385Q/+
p<0.05
Relative osk mRNA
56%
NS, p = 0.054
162%
p<0.001
194%

Figure 4

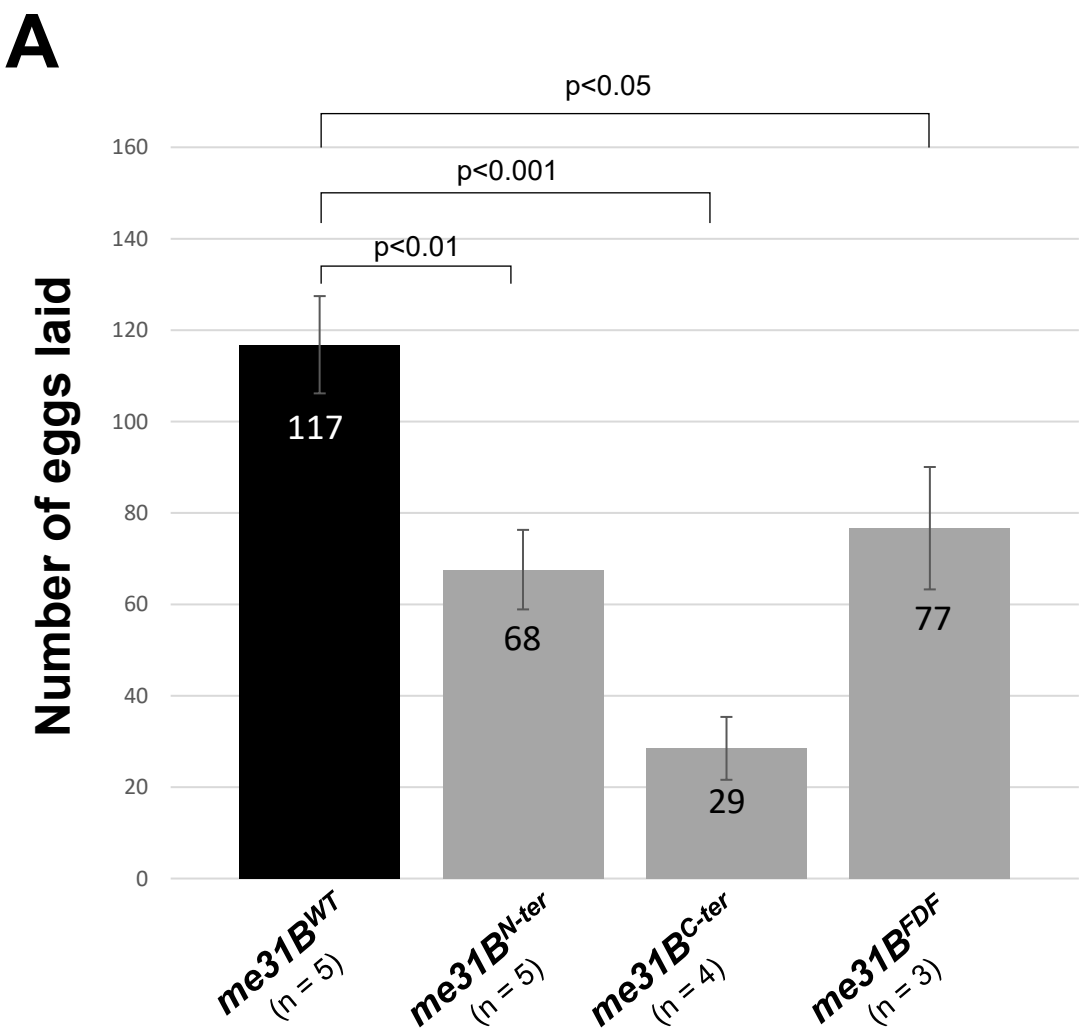
A
p<0.05
p<0.001
p<0.01
Number of eggs laid
160
140
120
100
80
60
40
20
0
117
68
29
77
me31B^WT (n = 5)
me31B^N-ter (n = 5)
me31B^C-ter (n = 4)
me31B^FDF (n = 3)

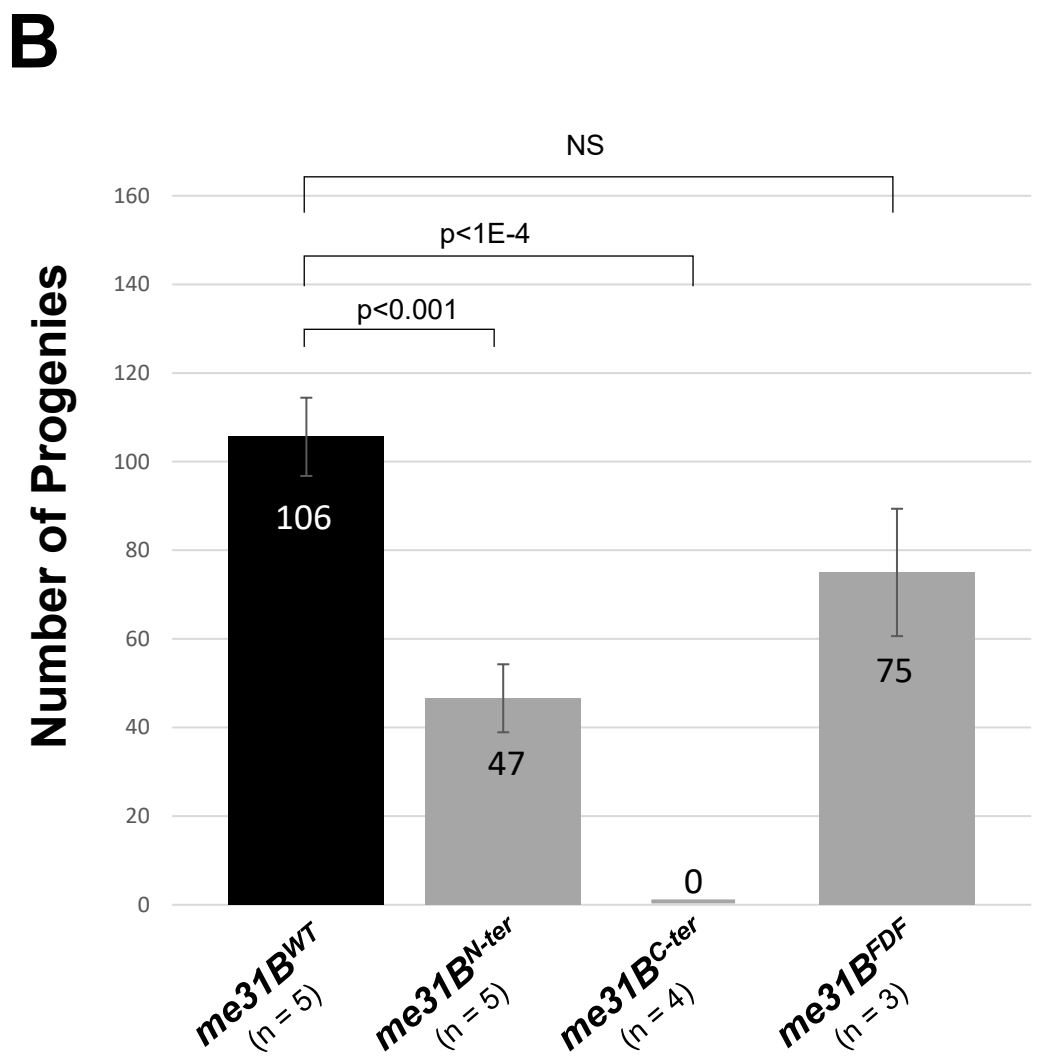
B
NS
p<1E-4
p<0.001
Number of Progenies
160
140
120
100
80
60
40
20
0
106
47
0
75
me31B^WT (n = 5)
me31B^N-ter (n = 5)
me31B^C-ter (n = 4)
me31B^FDF (n = 3)

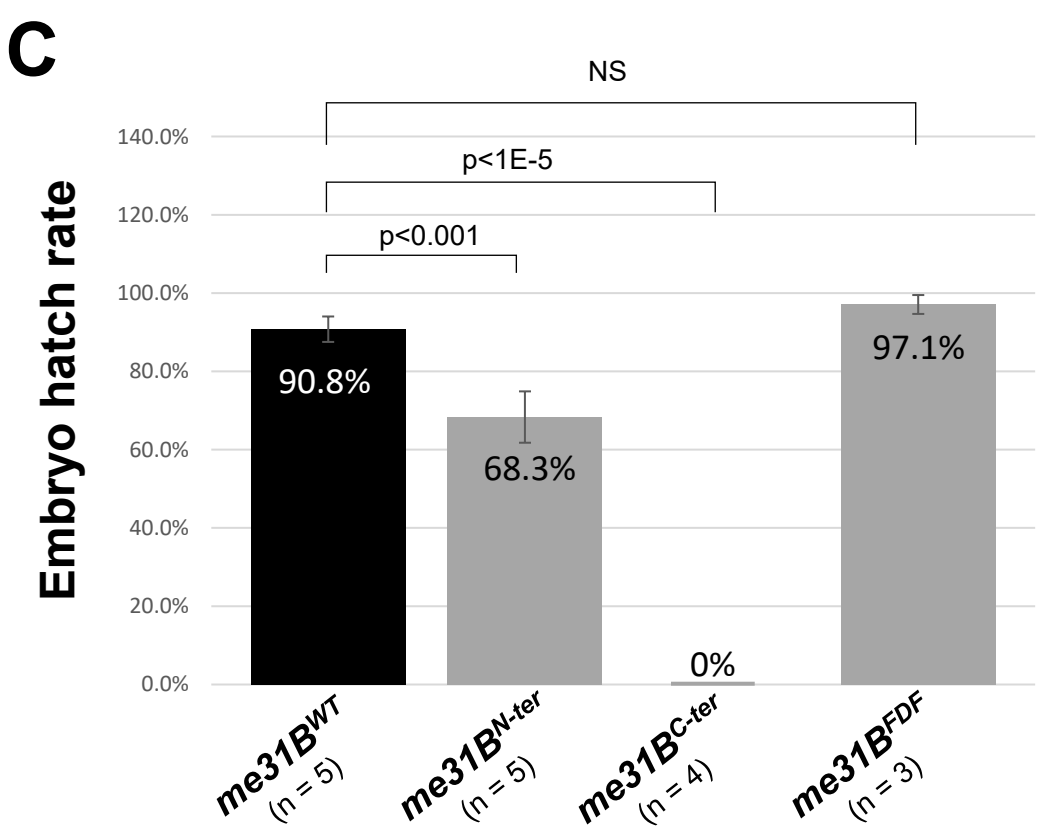
C
NS
p<1E-5
p<0.001
Embryo hatch rate
140.0%
120.0%
100.0%
80.0%
60.0%
40.0%
20.0%
0.0%
90.8%
68.3%
0%
97.1%
me31B^WT (n = 5)
me31B^N-ter (n = 5)
me31B^C-ter (n = 4)
me31B^FDF (n = 3)

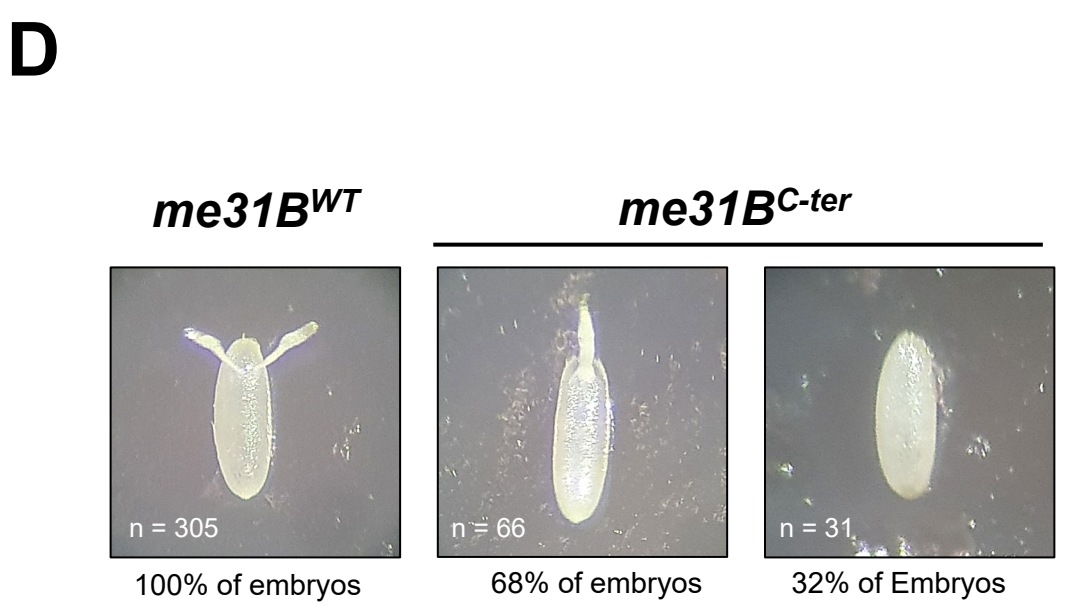
D
me31B^WT
me31B^C-ter
n = 305
n = 66
n = 31
100% of embryos
68% of embryos
32% of Embryos

Figure 5

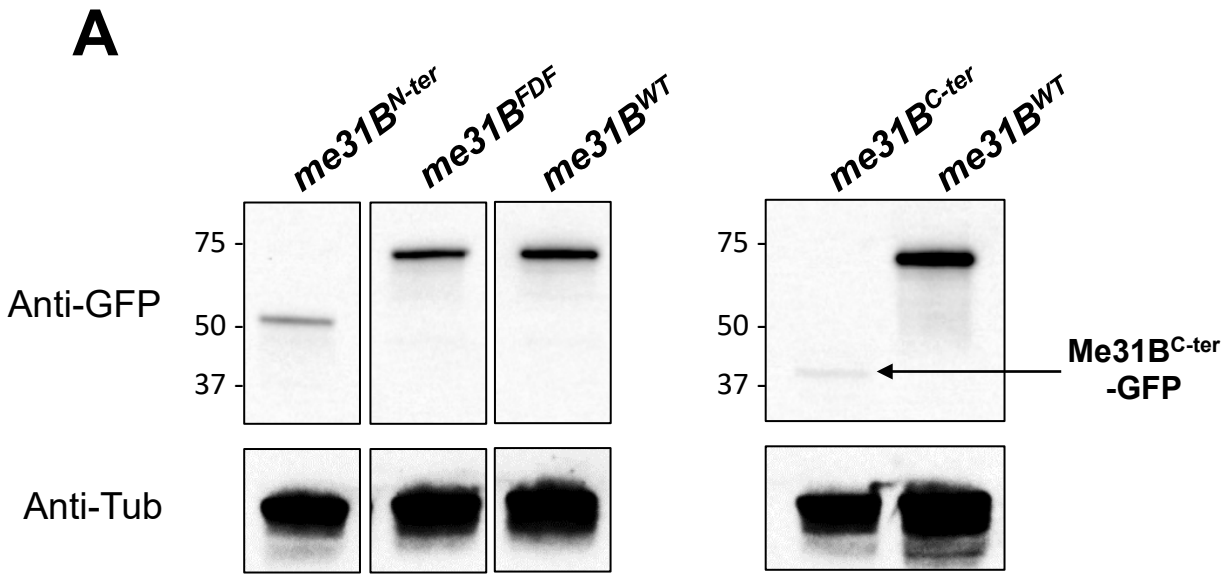
A
me31B^N-ter
me31B^FDF
me31B^WT
me31B^C-ter
me31B^WT
Anti-GFP
Anti-Tub
75
50
37
75
50
37
Me31B^C-ter -GFP

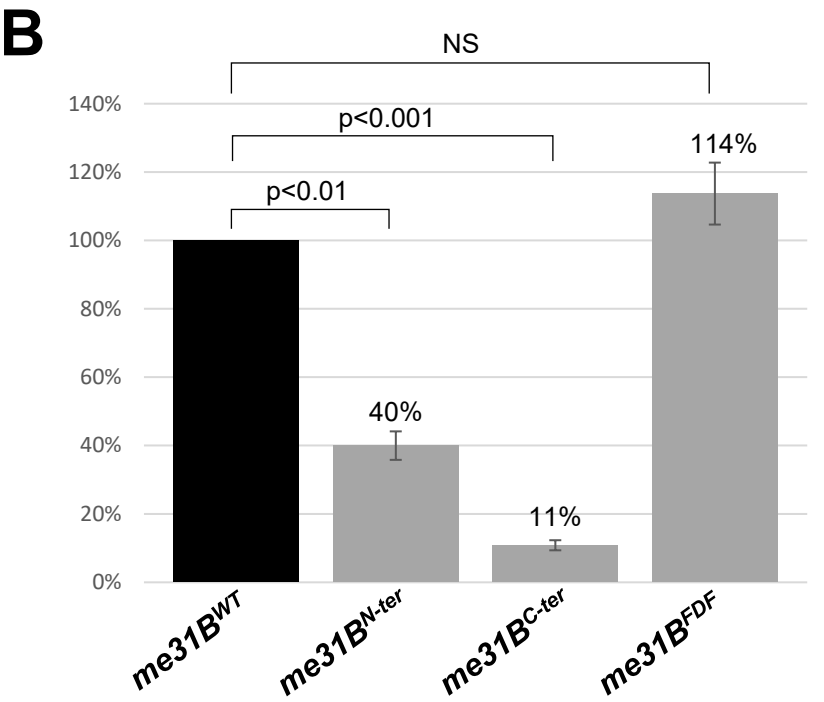
B
NS
p<0.001
p<0.01
140%
120%
100%
80%
60%
40%
20%
0%
114%
40%
11%
me31B^WT
me31B^N-ter
me31B^C-ter
me31B^FDF

Figure 6

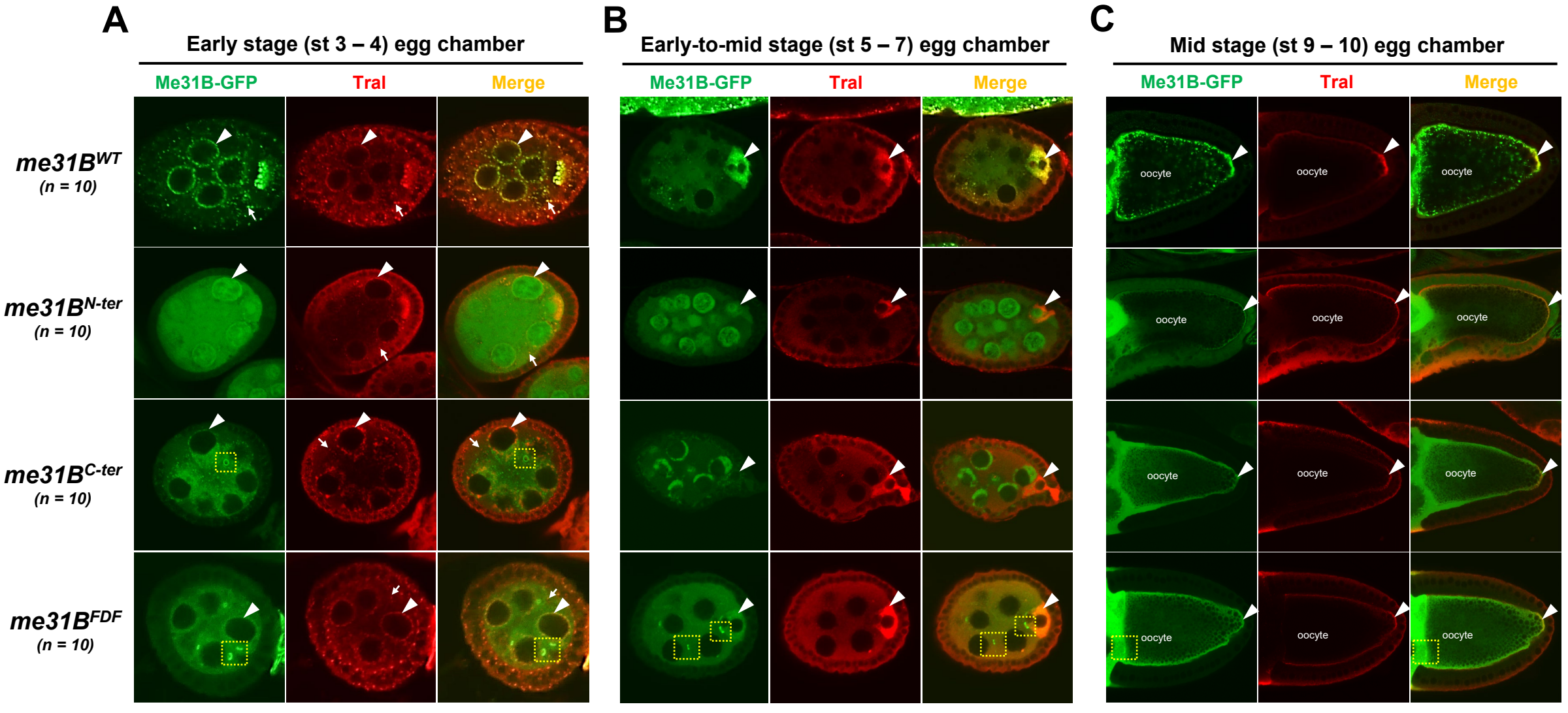
A
Early stage (st 3 – 4) egg chamber
Me31B-GFP
Tral
Merge
me31B^WT
(n = 10)
me31B^N-ter
(n = 10)
me31B^C-ter
(n = 10)
me31B^FDF
(n = 10)
B
Early-to-mid stage (st 5 – 7) egg chamber
Me31B-GFP
Tral
Merge
C
Mid stage (st 9 – 10) egg chamber
Me31B-GFP
Tral
Merge
oocyte

Figure 7

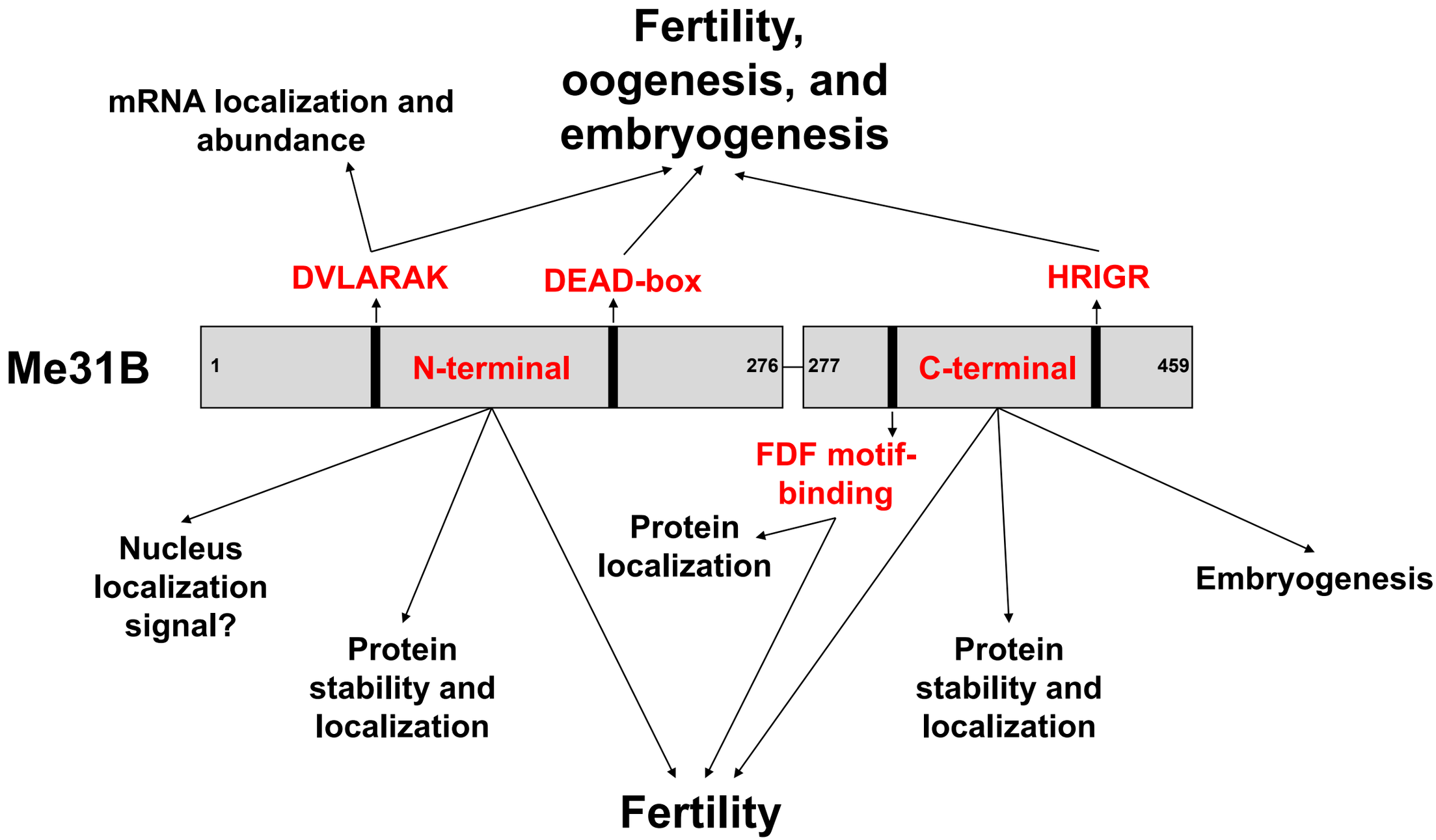
Fertility, oogenesis, and embryogenesis
mRNA localization and abundance
DVLARAK
DEAD-box
HRIGR
Me31B
1
N-terminal
276
277
C-terminal
459
FDF motif-binding
Nucleus localization signal?
Protein stability and localization
Protein localization
Protein stability and localization
Embryogenesis
Fertility